Master's thesis

NTNU
Norwegian University of Science and Technology
Faculty of Natural Sciences
Department of Physics

Kirsten Kristine Biering Mohr

Temperatures in the mesosphere and lower thermosphere and the viability of using non-continuous time series to derive tides

Master's thesis in MTFYMA
Supervisor: Patrick J. Espy
June 2022

NTNU
Kunnskap for en bedre verden

Kirsten Kristine Biering Mohr

Temperatures in the mesosphere and lower thermosphere and the viability of using non-continuous time series to derive tides

Master's thesis in MTFYMA
Supervisor: Patrick J. Espy
June 2022

Norwegian University of Science and Technology
Faculty of Natural Sciences
Department of Physics

NTNU
Norwegian University of
Science and Technology

Acknowledgement

I would like to thank my supervisor, Patrick J. Espy, for amazing guidance, helpful tips and tricks, and good humour. He has made it fun and perfectly challenging to work on this thesis. I would like to thank Anders for catering, company, and companionship in Bergen this year. A big hug is also sent to family in Oslo for offering a nice place to relax and disconnect. Finally, thank you to all my friends for keeping me sane this spring.

Summary

By using ground-based measurements of the hydroxyl (OH) and meridional wind over Trondheim, the temperatures for the (3,1) and (4,2) Meinel bands have been calculated. The calculations presented in this thesis are based on measurements done in 2021. The procedure was based on fitting a Gaussian to the intensity spectra, and a step-wise approach to this has been documented. In addition, conditions to determine the accuracy of the computational temperature calculations have been presented which depend on the relative root mean square error of the Gaussian fit relative to the standard variation in the temperatures. The temperatures are found to be in accordance with previous studies and show that the (3,1) temperature, on average, was slightly higher than the (4,2) temperature.

The tides in the temperatures were derived through a frequency analysis. Using hourly averages damped the effect of geophysical and statistical noise, but the power spectra were still difficult to interpret. This led to research on how non-continuous time series affect the tides derived through a Lomb-Scargle transform. The results showed that sampling data creates artificial tides that will confuse the conclusion if one is unaware of this effect. These results would make it possible to use cheaper measurement techniques to derive atmospheric tides. This thesis also presents results determining the necessary length of the sampled time as well as the length of the time series for the sampled non-continuous time series to be able to be used to derive tides. For example, if the sampled time is longer than fourteen hours, it is sufficient to use one night's worth of sampled data. If one has four subsequent days of sampled data, the nights need to be at least eight hours long.

Sammendrag

Ved å bruke bakkebaserte målinger av hydroksyl (OH) og meridional vind over Trondheim er temperaturene for (3,1) og (4,2) Meinel-båndene beregnet. Beregningene som presenteres i denne oppgaven er basert på målinger gjort i 2021. Prosedyren gikk ut på å tilpasse en Gaussisk funksjon til intensitetsspektrene, og en detaljert fremgangsmåte er dokumentert. I tillegg er det presentert betingelser for å bestemme nøyaktigheten av temperaturberegningene som avhenger av den relative feilen til kurvetilpasningen i forhold til standardvariasjonen i temperaturene. Temperaturene er funnet å være i samsvar med tidligere studier og viser at (3,1) temperaturen i gjennomsnitt var litt høyere enn (4,2) temperaturen.

Periodene i temperaturene ble utledet gjennom en frekvensanalyse. Bruk av timegjennomsnitt dempet effekten av geofysisk og statistisk støy, men frekvensspektrene var fortsatt vanskelige å tolke. Dette førte til en analyse av hvordan ikke-kontinuerlige tidsserier påvirker periodene fremskaffet gjennom en Lomb-Scargle-transformasjon. Resultatene viste at å samle data kun om natten skaper kunstige perioder som vil forvirre resultatene hvis man ikke er klar over denne effekten. Disse resultatene vil gjøre det mulig å bruke billigere måleteknikker for å utlede atmosfæriske svingninger og perioder. Denne oppgaven presenterer også resultater som bestemmer nødvendig lengde på den samlede måletiden samt lengden på tidsserien for at de ikke-kontinuerlige tidsseriene skal kunne brukes i en frekvensanalyse. For eksempel, hvis måleperioden er lengre enn fjorten timer, er det tilstrekkelig å bruke én natt med data. Hvis man har fire påfølgende dager med data, må nettene være minst åtte timer lange.

Table of Contents

Chapter 1

Introduction

Hydroxyl (OH) is an unstable molecule produced by ozone and hydrogen. OH exists in the atmosphere at altitudes between 80 to 110 kilometres, the region known as the mesosphere and lower thermosphere (MLT). Initially produced at high vibrational levels, hydroxyl relaxes through vibrational transitions and releases radiation in the infrared region which can be seen from space as airglow. The area of the atmosphere in which these processes happen is also the arena for strongly varying wind systems. These wind systems cause tides in the atmosphere, which are essential for coupling energy between the lower and upper atmosphere, and have been researched for many years.

In Trondheim (63.4°N 10.5°E), the OH is measured by a spectrometer, and a meteor radar measures the wind in the MLT-region. These measurement techniques differ in performance, price, and infrastructure requirements. The meteor radar is very costly to operate and requires a large area and a lot of infrastructure, while the spectrometer is relatively cheap, small, and easy to operate. In addition, OH is produced at night, leaving the spectrometer operating only when the sun has set.

This thesis aims at calculating the temperatures for the (3,1) and (4,2) Meinel bands by using OH measurements. From these calculations, the tides in the temperature can be derived. Since the OH intensity is measured by a ground-based spectrometer which needs a clear night sky to get good measurements, the number of days applicable for this kind of analysis is limited. This thesis considers how the different measurement techniques affect the derivation of tides.

Since tides are such a significant part of atmospheric physics, an analysis of the derivation of tides is interesting as it evaluates how data analysis can produce misleading and artificial results. Such an analysis will comment on previous studies in this field. In addition, this research can be elaborated on to create a way to analyse tides from non-continuous time

series. An example is being able to use a time series produced by measuring OH at night only, compared to using a continuous time series created by continuously measuring the wind. This may create a cheaper solution to deriving tides in the atmosphere, as it would be possible to rely on a spectrometer and not a meteor radar.

This thesis presents the theory behind the production and radiation of the OH molecule and the dynamic processes creating the wind. Since the thesis is heavily based on work done in a previous project report (Mohr 2021), much of the theory describing the chemical and dynamical processes, instrumentation description and data handling is extensively taken from that report. It includes a detailed orientation of how the atmospheric temperatures are calculated based on OH intensities and presents a few temperature calculations on the temperature in the MLT above Trondheim. Tides in the temperature are derived, followed by an analysis of the viability of using non-continuous time series to derive tides. Finally, some requirements for the measured data are presented, as well as future work on the area.

Chapter 2

Theory

This theory lays the foundation for understanding the following discussions surrounding the calculated results. Since this master thesis is heavily based on the project report (Mohr 2021), part of the theory is extensively taken from that report, particularly section 2.1, section 2.2, section 2.3, section 2.4, and section 2.6.

2.1 The atmosphere and atmospheric structure

In the earth's atmosphere, the gasses nitrogen (N_2) and oxygen (O_2) are the predominating species. Other constituents such as carbon dioxide (CO_2), water vapour (H_2O) and ozone (O_3) play an essential role in the heath transfer, radiation and reflection of ultraviolet light from the sun, the seas and land (Andrews 2010). The earth's atmosphere has been divided into four primary horizontal layers, defined by the temperature gradient. The temperature gradient is a measurement of how the temperature changes in relation to the height above ground.

Closest to earth is the troposphere, which reaches from the ground up to around 15km. The ground is heated by sunlight, and as the air cools, the temperature decreases. Consequently, it is characterised by a negative temperature gradient. The troposphere contains about 80% of the total atmospheric mass. The weather phenomena occur in this region of the atmosphere, as 99% of all water vapour exists here (*Atmospheric Structure* n.d.).

The troposphere gives way to the tropopause, a band ranging from 8 - 11km in height. The tropopause is replaced by the stratosphere that reaches the stratopause at 45km. About 90% of all ozone is in the stratosphere. The ozone's absorption of ultraviolet (UV) radiation from the sun causes the temperature to increase and results in a positive temperature

gradient.

The mesosphere is bounded by the mesopause, a 10-kilometre region, which is also the coolest region in the atmosphere. The mesosphere layer ranges from the stratopause to about 85km above the ground. The temperature decreases with altitude due to reduced solar heating and increased radiation to space (Andrews 2010).

After the mesopause there is the thermosphere. The thermosphere is characterised by increasing temperatures with altitude and therefore a positive temperature gradient. This is because the little solar radiation remaining is absorbed by the few atoms and molecules existing in this region. Due to the tilt and rotation of the earth around the sun, the solar radiation will vary through the seasons, leading to the temperature ranging between 600 and 2000K. The exosphere is the final section, and upward travelling gasses escape the earth's gravity. This region depends on solar radiation and will exist from 250-200 kilometres above ground.

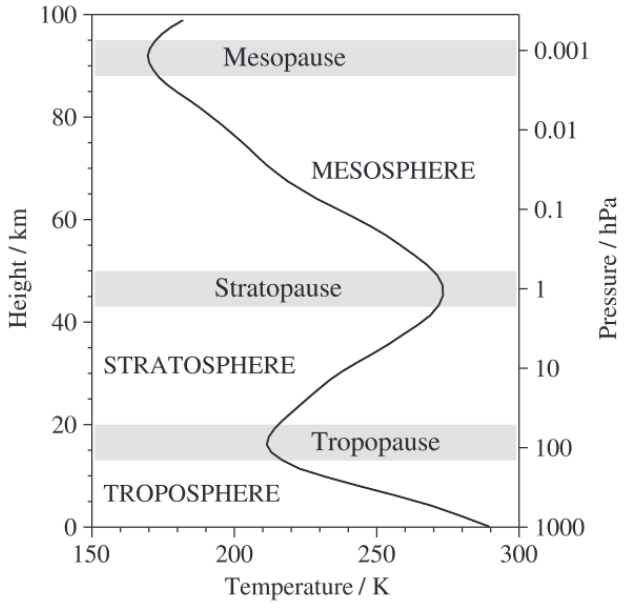

Figure 2.1: The Atmospheric structure and temperature profile. The figure is taken from Andrews 2010.

2.2 OH production

The hydroxyl molecule, OH, is found in the upper mesosphere and lower part of the thermosphere. It peaks at around 88km with a half-width of 6-8km (Lowe et al. 1996).

Excited hydroxyl is produced by the reaction described by Marsh et al. 2006, seen in equation (2.1), where hydrogen and ozone combine into an unstable, excited state of the hydroxyl molecule.

$$H + O_3 \longrightarrow OH^* + O_2. \tag{2.1}$$

The excited state of the hydroxyl (OH^*) is then de-excited through a decrease in vibrational modes to a more stable state, OH (see section 2.3). This de-excitation causes the OH molecule to emit radiation viewed as airglow, a glowing layer in the upper atmosphere visible from space. Marsh et al. 2006 presented how the amount of OH in the atmosphere is dependent on the amount of hydrogen and ozone present, as can be seen clearly in figure 2.3. The oxygen in the OH is the atomic oxygen produced when UV radiation splits ozone during the day. Therefore, the OH population can be calculated by knowing the atomic oxygen density, molecular oxygen density, and hydrogen density in the atmosphere. The ozone density at night time is dependent on the recombination of atomic oxygen and the losses with atomic hydrogen:

$$[O_3] = \frac{k_{O+O_2+M}[O]\,[O_2]\,[M]}{k_{H+O_3}[H]}. \tag{2.2}$$

This leaves the production rate for excited OH^*

$$P\,(OH^*) = k_{H+O_3}[H]\,[O_3]\,. \tag{2.3}$$

By combining equation (2.2) and equation (2.3), the production rate of hydroxyl is proportional to the atomic oxygen concentration

$$P\,(OH^*) = k_{O+O_2+M}[O]\,[O_2]\,[M]. \tag{2.4}$$

Atomic oxygen is mainly produced by the destruction of ozone by the use of ultraviolet light.

$$O_3 + h\nu = O_2 + O. \tag{2.5}$$

This happens in the daytime, as it requires sunlight. The recombination process takes a while and will continue through the night. The intensity of OH will therefore decrease through the night, as the available O and O_2 are decreasing due to the production of O_3. Figure 2.2a shows how the OH intensity typically varies through a night with no clouds over Trondheim.

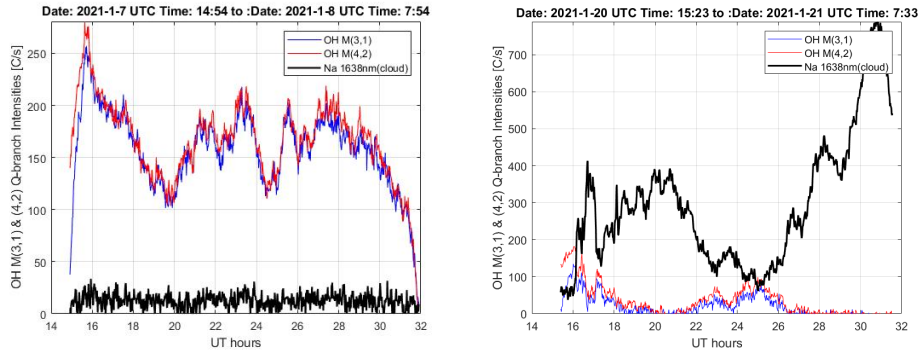

(a) Typical OH intensity over Trondheim on a cloudless night for the (3,1) and (4,2) Meinel bands and the Na-intensity.

(b) Example of how the OH intensity for the (3,1) and (4,2) Meinel bands behaves when there are clouds (Na > 50 counts/second).

Figure 2.2: Examples of the OH intensity for the (3,1) and (4,2) Meinel bands and the Sodium intensity. When Na is below 50 counts per second, the OH measurements are considered good. An anti-correlation between the OH and Na intensity can be observed when the Na intensity increases above this.

The distribution of the atmospheric components used in the production of OH can be seen in figure 2.3. This example, along with the vibrational emission rate of the different bands (figure 2.8), is calculated using the MSIS model (Hedin 1991) and an unpublished atmospheric model. The MSIS model provides the background atmosphere, and the ozone density was computed using equation (2.2) by knowing the O, O_2 and total number density M. The MSIS was run as an average over the 7th of January 2022 (a night defined for solar zenith angles greater than 95 degrees). With the ozone calculated, the density of each vibrational state of the OH is calculated by using equation (2.3), equation (2.4), and quenching, described in more detail in section 2.4.

2.3 Spectroscopy of diatomic molecules

To understand how and why the excited hydroxyl molecule can result in airglow, it is necessary to understand some basic quantum mechanics of diatomic radicals.

The energy of a molecule can be expressed as a sum of electronic energy, rotational energy, and vibrational energy.

$$E = E_e + E_r + E_v \tag{2.6}$$

The electronic energy E_e is associated with the electromagnetic forces used to hold together the molecule. E_r is the energy resulting from the molecule's rotation, and E_v is the

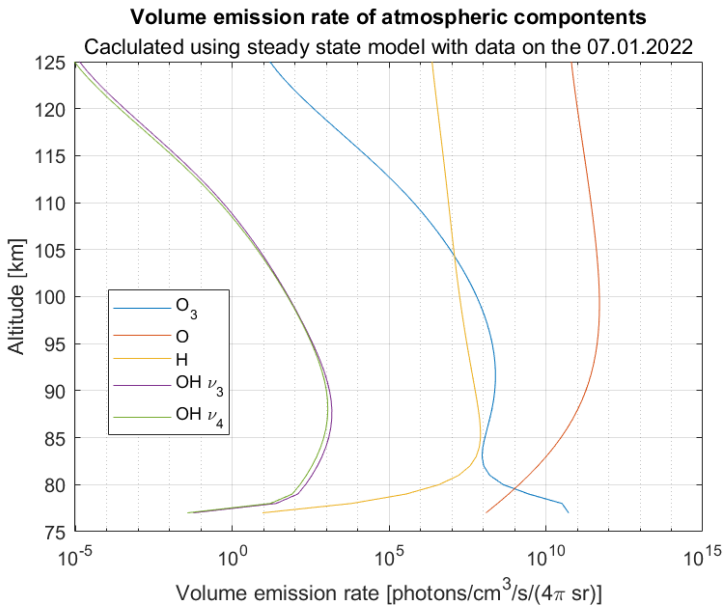

Figure 2.3: The volume emission rate of the atmospheric components used in the production of OH. The emission rate of the (3,1) and (4,2) OH bands follows the distribution of O_3 and H. Data provided by P. Espy through personal communication.

result of the internal vibrational energies in the molecule. The energies have the properties $E_v \ll E_r \ll E_e$, and the difference in frequencies and subsequent time scale is so big that each energy can be considered separately from the others. Three kinds of energy spectra correspond to each energy: Rotational, rotation-vibration, and electronic spectra.

There can be different vibrational and rotational states for one given electronic state. The theory described below is heavily based on (Herzberg 1971), specifically chapter 2, ”Diatomic radicals and ions”. A similar theory can be found in any textbook about quantum mechanics, such as Hemmer 2005.

2.3.1 The rotational spectra

The rotation spectra is the transition from one rotational level in a given vibrational and electric state to another rotational level in the same vibrational and electric state.

The simplest way to describe the rotational energy spectrum is to envision a dumbbell model: two masses m_1 and m_2 separated by a massless rod with length r. Classical mechanics then states that the rotational energy of the system is

$$E_r = \frac{1}{2} I \omega^2. \tag{2.7}$$

ω is the angular velocity, and I is the moment of inertia, defined as

$$I = m_1 r_1^2 + m_2 r_2^2 = \mu r^2, \tag{2.8}$$

where $r = r_1 + r_2$ and

$$\mu = \frac{m_1 m_2}{m_1 + m_2} \tag{2.9}$$

is the reduced mass. The angular momentum, P, of the system is then

$$P = I\omega, \tag{2.10}$$

which reduces the energy to

$$E_r = \frac{P^2}{2I}. \tag{2.11}$$

By looking at the energy solution from a quantum mechanical perspective, it is clear that the energy can only take specific discrete values. These can be found by solving the Schrödinger equation. The most widely known solution is

$$E_r = \frac{h^2}{8\pi^2 \mu r^2} J(J+1) = \frac{h^2}{8\pi^2 I} J(J+1). \tag{2.12}$$

J is the quantum rotational number and can take values $J = 0, 1, 2, ...$

The quantum number is related to the angular momentum by the equation

$$|\boldsymbol{P}| = \frac{h}{2\pi} \sqrt{J(J+1)}. \tag{2.13}$$

By substituting equation (2.13) into equation (2.7), equation (2.12) will follow.

In molecular spectroscopy, relevant for this thesis, the energy is usually depicted in term values, [cm^{-1}], which is obtained by dividing by hc. h is Planck's constant, and c is the speed of light in a vacuum.

$$F(J) = \frac{E_r}{hc} = BJ(J+1), \tag{2.14}$$

with

$$B = \frac{h}{8\pi^2 cI} = \frac{h}{8\pi^2 c\mu r^2}. \tag{2.15}$$

B is called the rotational constant, and $F(J)$ is depicted in term values.

If the molecular form allows for small deformations when rotating, the centrifugal force will also play a part in the rotational energy. The rotational term-value then takes the form

$$F(J) = BJ(J+1) - DJ^2(J+1)^2 + \cdots, \tag{2.16}$$

where B is as stated in equation (2.15), and D is a small correction term, approximately

$$D = \frac{4B^3}{\omega^2}. \tag{2.17}$$

2.3.2 The vibrational spectra

As a good first approximation, the vibration of a diatomic molecule can be expressed as a harmonic oscillator. By operating with reduced mass, equation (2.9), and a displacement $x = r - r_e$ from the equilibrium position, the potential energy of the system becomes

$$V = \frac{1}{2}kx^2 = \frac{1}{2}k\left(r - r_e\right)^2. \tag{2.18}$$

The force constant, k is related to the vibrational frequency ν by

$$k = 4\pi^2\mu\nu^2. \tag{2.19}$$

Solving the Schrödinger equation for the harmonic oscillator makes it clear that the vibrational energy, as for the rotational energy, can only take discrete values.

$$E_\nu = h\nu(\nu + \frac{1}{2}), \tag{2.20}$$

where $\nu = 0, 1, 2, ...$ In term values ([cm^{-1}]), the vibrational energy becomes

$$G(v) = \frac{E_v}{hc} = \omega \left(v + \frac{1}{2} \right), \tag{2.21}$$

where $\omega = \frac{\nu}{c}$ is the vibrational frequency.

Unlike a perfect harmonic oscillator, a diatomic molecule will not be able to expand r to infinity. Instead, the spring force will reach a constant value, called an anharmonic oscillator. The potential can be expressed as

$$U = f\left(r - r_e\right)^3 - g\left(r - r_e\right)^3 + \ldots, \tag{2.22}$$

and by solving the Schrödinger equation, it will yield the term values

$$G_0(v) = \omega_0 v - \omega_0 x_o v^2 + \omega_0 y_0 v^3 - \ldots, \tag{2.23}$$

with zero-energy $v = 0$. x_0 and y_0 is smaller than one, and $g \ll f$.

If there exists a dipole moment in the molecule, electrodynamics states that a photon with a frequency equal to the vibrational frequency will be emitted or absorbed by the molecule. The wavenumber will be

$$\nu = \frac{E\left(v'\right)}{hc} - \frac{E\left(v''\right)}{hc} = G_0\left(v'\right) - G_0\left(v''\right). \tag{2.24}$$

A harmonic oscillator only allows for wavenumbers $\Delta v = \pm 1$, while an anharmonic oscillator allows $\Delta v = \pm 2, \pm 3, ...$

2.3.3 Rotational-vibrational spectrum

In reality, a molecule will vibrate and rotate simultaneously, and the interaction of these two energies must be considered. There can be transitions from a rotational level for a given vibrational level to a different rotational level at a new vibrational level, all for the same electric state. When this occurs, there will be a rotational-vibrational spectrum.

When a molecule vibrates, the distance r changes, and so will the moment of inertia (2.8). This will change the rotational constant, $B = B_\nu$, for a specific vibrational level compared to the rotational constant $B = B_e$ for the same system in equilibrium position. It is possible to find B_ν by averaging over the different internuclear distances r.

$$B_\nu = \frac{h}{8\pi^2 c\mu}\left[\frac{1}{r^2}\right]_{\text{avg}}, \tag{2.25}$$

which will give

$$B_\nu = B_e - \alpha_e\left(\nu + \frac{1}{2}\right) + \ldots, \tag{2.26}$$

with

$$B_e = \frac{h}{8\pi^2 c\mu r_e^2}. \tag{2.27}$$

α_e is a small constant compared to B_e and depends on the anharmonicity of the vibrations. Similarly, there will be a corrected rotational constant

$$D_\nu = D_e + \beta_e\left(\nu + \frac{1}{2}\right) + \ldots, \tag{2.28}$$

where D_e is the rotational constant at equilibrium.

When the interaction between rotation and vibration is taken into account, the term value will become

$$F_\nu(J) = B_\nu J(J+1) - D_\nu J^2(J+1)^2 + \ldots, \tag{2.29}$$

where the subscript ν refers to which vibrational level to consider.

J and ν are still governed by quantum mechanics and must take discrete values. By considering $\Delta\nu = 0$, the system will behave in a pure rotational spectrum. By looking at a transition from upper state J' to lower state J'' and using the term value to account for the rotational and vibrational part, the result becomes

$$\nu = \nu_0 + B'_v J'\left(J'+1\right) - B''_v J''\left(J''+1\right) \tag{2.30}$$

Here, ν_0 is the wavenumber of a pure vibrational ($\Delta J = 0$) transition.

Since $\Delta J = J' - J''$ can take the values 0 and ± 1, there will occur a branching of the transitions. These branches are called the Q-branch, P-branch and R-branch.

The *Q-branch* happens when $\Delta J = 0$. By choosing $J' = J'' = J$, equation (2.30) becomes

$$\nu_Q = \nu_0 + (B'_\nu - B''_\nu)\, J + (B'_\nu - B''_\nu)\, J^2. \tag{2.31}$$

When $\Delta J = 1$, the transition is called the *R-branch*. By having $J'' = J$ and $J' = J + 1$, the wave number becomes

$$\nu_R = \nu_0 + 2B'_\nu + (3B'_\nu - B''_\nu)\, J + (B'_\nu - B''_\nu)\, J^2 \tag{2.32}$$

The *P-branch* occurs when $\Delta J = -1$. For this to happen, $J'' = J$ and $J' = J - 1$. The wave number for the P-branch then becomes

$$\nu_P = \nu_0 - (B'_\nu + B''_\nu)\, J + (B'_\nu - B''_\nu)\, J^2. \tag{2.33}$$

The relation between the vibrational levels ν (in the figure depicted by *v*), the different rotational transitions, and its connection to the P-, Q-, and R-branches can be seen in figure 2.4.

These three equations describe how the different branches will behave as J develops. When $B''_\nu > B'_\nu$, ν_Q will decrease slowly as J increases. Since $B'_\nu - B''_\nu$ is a very small factor, the lines will be located very close together, and be seen as one Q-branch (figure 2.5). The R-branch's wavenumber will increase as J increases until the factor J^2 becomes large enough, at which point the ν_R will begin to decrease. The P-branches with wavenumber ν_P will always decrease with increasing J. The lines are easier to discern because of the term $B'_\nu + B''_\nu$.

Due to the total electron spin vector, one has to take the angular momentum of the electrons into account. This leads to corrections in the dumbbell model, and the effect creates a splitting of the lines. The electronic state of the molecule determines this split. The state of the molecule can be $\Lambda = 1/2$ or $\Lambda = 3/2$. The transition between such two states gives rise to a splitting of the bands. Photons in the same branch created by a transition with the same ΔJ can have different lines in the branch. The branches with their corresponding peaks in the intensity spectra, and J''- and N''-values can be seen in figure 2.4. N'' is the integer quantum number, while J'' is the sum of nuclear and electron spin angular momentum, as opposed to in section 2.3.1 where Herzberg 1971 considered J to be the angular momentum without spin.

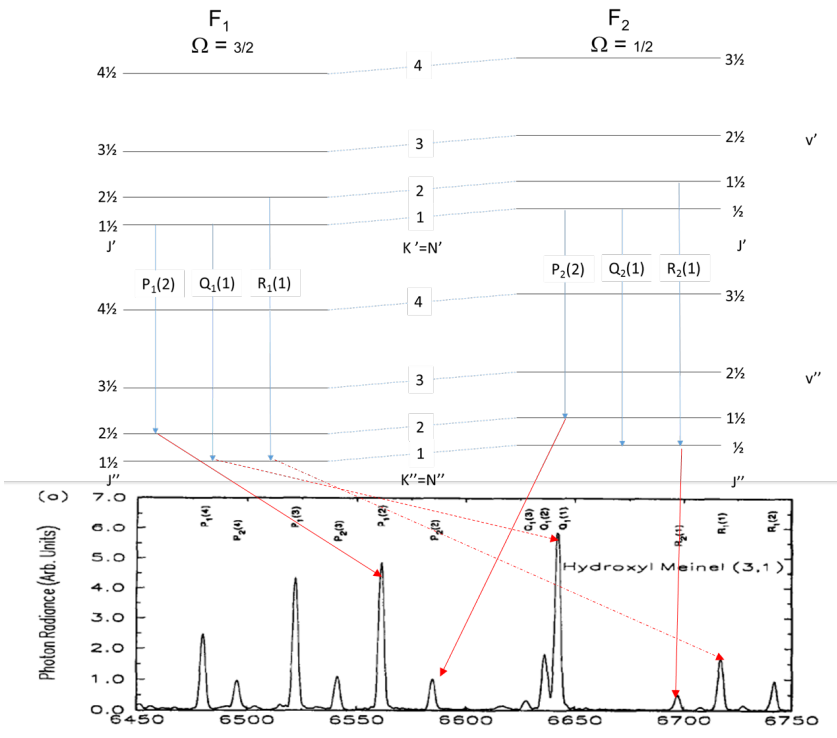

Figure 2.4: The different transitions between vibrational and rotational states and the corresponding peaks in an OH (3,1) intensity spectra. $\Omega = 3/2$ refers to the P_1-lines, and $\Omega = 1/2$ refers to the P_2-lines. x'' refers to the upper level of the relevant entity (x used as a placeholder), while the x' refers to the lower level. J is the sum of nuclear and electronic spin and is half-integer, while N is the integer quantum number. Figure from P. Espy through personal communication.

2.4 Meinel lines

The Meinel lines are emission bands discovered by A. B. Meinel in 1950 (Meinel 1950). The bands are a result of the rotational-vibrational spectra of OH. The initial production of OH^* given by equation (2.5) produces OH^* with vibrational states $\nu = 6$ up to $\nu = 9$ (Sivjee 1992). The molecule will then radiate and end up in a more stable version of OH with lower vibrational levels. In addition to OH radiating and cascading to a lower vibrational level, it can also happen through a stepwise collision quenching (equation (2.34)) with other molecules in the air, namely N_2, O_2 and O. (Sivjee 1992) proposes that this happens by "sudden death" (equation (2.35)):

$$OH^*(v') + M \rightarrow OH^*(v' - 1) + M \tag{2.34}$$

$$OH^*(v') + M \rightarrow OH^*(v' = 0) + M \tag{2.35}$$

This thesis will focus on the Meinel lines (3,1) and (4,2). In this is understood the transition between the vibrational level $\nu = 3$ to $\nu = 1$, and $\nu = 4$ to $\nu = 2$. The intensity spectra as a function of wavelength can be seen in figure 2.5, and the nightly intensity of the Q-branches in the bands can be seen in figure 3.3. As described above, each band has three rotational branches, P, Q, and R-branches. With the resolution of the spectrometer in Trondheim, it is difficult to discern between the different lines in the R-branch. The P-lines on the other hand, are clearly defined. The different lines are denoted $P_{1,2}(N'')$. $N'' = J'' \pm 1/2$ is the integer quantum number. The subscript is either 1 or 2 and refers to the electronic state of $^2\Pi_{3/2}$ and $^2\Pi_{1/2}$. $P_1(N'')$ refers to the $^2\Pi_{3/2}$-state with $N'' = J'' - 1/2$, and are the strongest lines, while $P_2(N'')$ refers to $^2\Pi_{1/2}$ with $N'' = J'' + 1/2$. The strengths of the different lines can be seen in figure 2.5. J'' and N'' will be used interchangeably, and will always refer to the upper rotational state.

Since $\Delta J = -1$ for the P-branches, and J can not be zero in a Π-state, the first line in the P-branch is the $P_2(2)$-line. From there on follows the $P_1(2)$-line, the $P_2(3)$-line etc. Since the first five rotational states in the P-lines are easy to discern with the spectrometer in use, these lines will be used in this thesis when calculating the rotational temperature of the different Meinel bands.

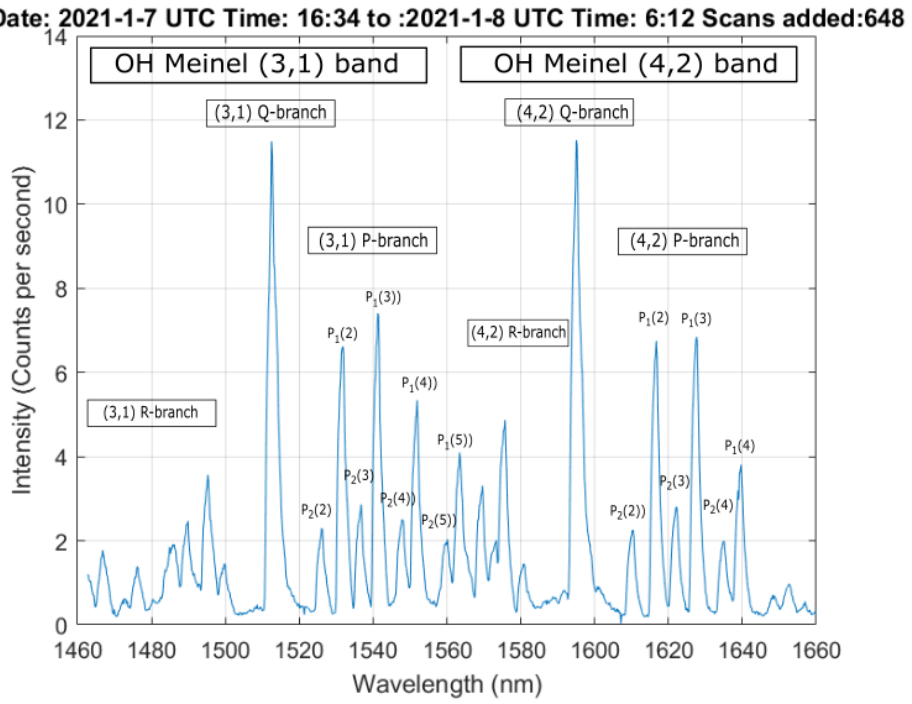

Figure 2.5: The averaged OH intensity spectrum on the night 7.01-8.01.2021. The R-, P-, and Q-branches in the (3,1) and (4,2) Meinel bands are visible in this wavelength range.

Figure 2.2a gives an example of how the OH intensity of the (3,1) and (4,2) Meinel band

varies throughout the night. (P J Espy and Stegman 2002) present seasonal variance in the intensity of OH radiance. This can be seen in figure 2.6 and shows how the (3,1)-band intensity varies through the year. In addition to this, figure 2.7 depicts the density distribution of the OH at different vibrational levels. This has been produced by using the atmospheric model described in section 2.2. As can be seen, the $\nu' = 3$ is the third vibrational level and has a maximum at a slightly lower altitude than the fourth vibrational level, $\nu' = 4$. The OH varies not only through the night (figure 2.2a), it varies quite a lot during the year (figure 2.6) and depending on which vibrational level one considers (figure 2.7).

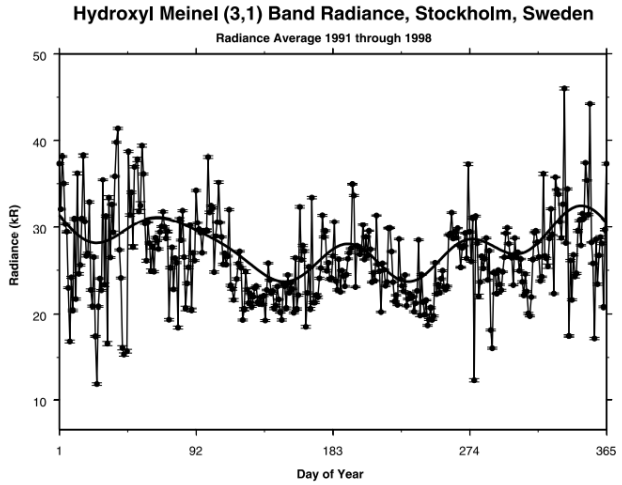

Figure 2.6: Average yearly OH intensity variation over Stockholm, Sweden. The figure is from P J Espy and Stegman 2002. The radiance is in kiloreyleighs, with $1kR = \frac{10^9}{4\pi}[\frac{photons}{cm^2 \cdot sec \cdot sr}]$ (Baker et al. 2001).

2.5 Temperatures from the OH intensity

Different studies on the temperature in the upper mesosphere and lower thermosphere have been made, both connecting temperature and wind (Hennum and P. Espy 2013), and temperature and OH radiation (P. J. Espy et al. 2003). The temperature in the atmosphere can be found by using the OH intensity through the equation

$$I_J = N_0 A 2(2J+1) \exp \frac{-\epsilon_J}{kT}. \tag{2.36}$$

I_J is the measured intensity, N_0 is the OH density, A is the Einstein coefficient, also known as the transition probability, and 2(2J+1) is the degeneracy in the upper rotational state. ϵ_J is the energy in the upper rotational state, k is Boltzmann's constant,

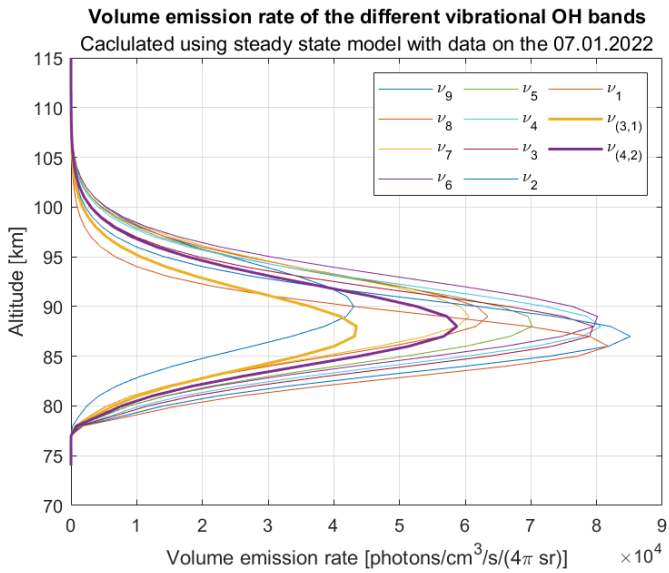

Figure 2.7: Volume emission rate distribution of the OH at different vibrational levels (ν). $\nu = 3$ has a maximum density at a lower altitude than $\nu = 4$. P. Espy provided data through personal communication by using the MSIS model and an unpublished atmospheric model on the 7th of January 2022.

$k = 0.695\,03\,\mathrm{cm}^{-1}/\mathrm{K}$, and T is the temperature. The tabulated values can be found in table 2.1. These values are taken from the HITRAN database (HIgh resolution TRANsmission molecular absorption database) (Rothman et al. 2013).

By taking the natural logarithm of both sides and rearranging it, the equation takes the form

$$\ln\left(\frac{I_J}{N_0 A 2(2J+1)}\right) = -\frac{\epsilon_J}{kT}. \tag{2.37}$$

The spectrometer in Trondheim has a resolution that makes it possible to isolate the main Q-branch and the P-branches with $J'' = 1$ to 5 for the (3,1) and (4,2) Meinel lines (as can be seen in figure 2.5). By applying the equation (2.37) which relates the peak intensity with temperature, it is possible to estimate the temperature by considering the (3,1) and (4,2) Meinel lines separately.

One can integrate over the specific peak for each branch to acquire the intensity and use tabulated values for the Einstein coefficient, degeneracy and energy for that branch. Taking the natural logarithm of the intensity divided by the line strength and plotting this against $\frac{\epsilon_J}{k}$ for every branch, a fitted curve through these points will have the slope $-1/T$.

Line	**Einstein coefficient** A	$\mathbf{E}_{J''}$ cm^{-1}	**Degeneracy** $2(2J''+1)$
(3,1)			
$P_1(2)$	23,67	10210,5669	8
$P_1(3)$	28,96	10285,4527	12
$P_1(4)$	31,18	10390,9803	16
$P_1(5)$	32,50	10527,5077	20
$P_2(4)$	34,26	10481,6516	12
$P_2(5)$	34,34	10605,4579	16
(4,2)			
$P_1(2)$	41,79	13287,1845	8
$P_1(3)$	51,20	13359,1251	12
$P_1(4)$	55,17	13460,4343	16
$P_2(3)$	61,50	13467,2951	8
$P_2(4)$	60,63	13552,4750	12

Table 2.1: The HITRAN values for the (3,1) and (4,2) Meinel bands. J'' represents the upper levels.

By using data from the model seen in figure 2.7 on the 7th of January 2022 for the individual band volume emission rate, it can be calculated that the average temperature for the (3,1) band is 205.299K, and for the (4,2) band it is 204.766K. These temperatures are in accordance with figure 2.9 if one looks at day number 7 in the northern hemisphere (NH). Temperature calculations using this data also return decreasing temperatures for increasing vibrational bands. The same model gives the temperature profile for mid-winter as a function of altitude, along with the volume emission rate of the (3,1) and (4,2) Meinel bands. This can be seen in figure 2.8.

(P J Espy and Stegman 2002) presents a variation in the mesospheric temperature at high altitudes through the year. These trends include a general seasonal change in temperature and monthly variations. Figure 2.9 shows how the temperature changes over Trondheim through the years. The change is more rapid during autumn than during spring.

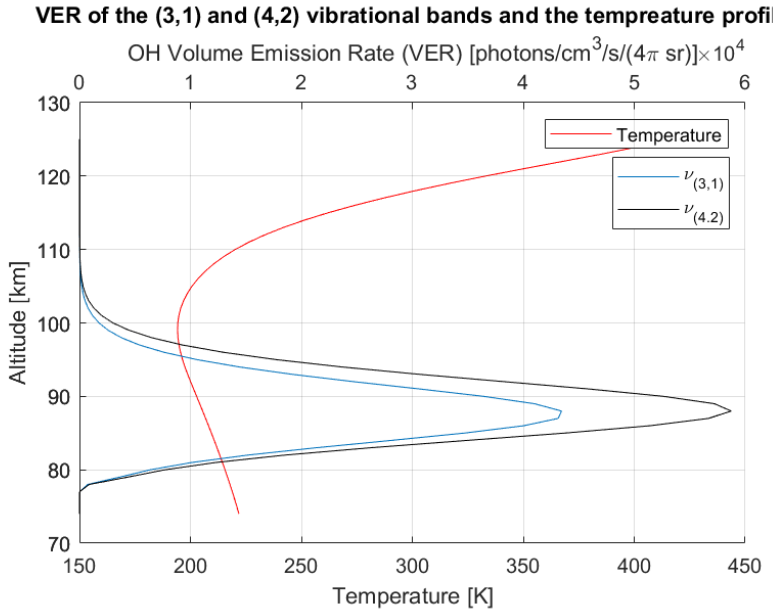

Figure 2.8: The temperature profile for mid-winter, along with the (3,1) and (4,2) volume emission rates (VER), as a function of altitude.

2.6 Wind and gravity waves

Wind can be divided into the zonal wind and meridional wind. Zonal wind represents the wind moving along longitudinal lines, namely in the east-west direction. The meridional flow is winds moving along the latitudinal circles, north to south. The meridional winds will generally move northwards during winter and towards the equator during summer (Andrews 2010). The meridional circulation, including vertical transportation of energy, is considered a more conceptually important energy circulation in the atmosphere than the more rapid zonal energy flows (Andrews 2010). The solstitial circulation of the atmosphere is driven by the deposition of momentum from gravity waves propagating upward from the lower atmosphere and has important implications for the transport of chemicals in the atmosphere (Andrews 2010).

The wind in the atmosphere is not a stable force but will change intensity and direction throughout the day in addition to solstitial circulations. The oscillations in the atmosphere, which have periods within one day, 24 hours, are called atmospheric tides. The 24-hour component is called the diurnal tide, and the 12-hour component is called the semi-diurnal tide (Lindzen 1979). When these two tides interact, an 8-hour wave will appear. This 8-hour tide is called the terdiurnal tide. When analysing winds on an interval over a couple of days, these diurnal, semi-diurnal and terdiurnal waves will show through a Fourier analysis

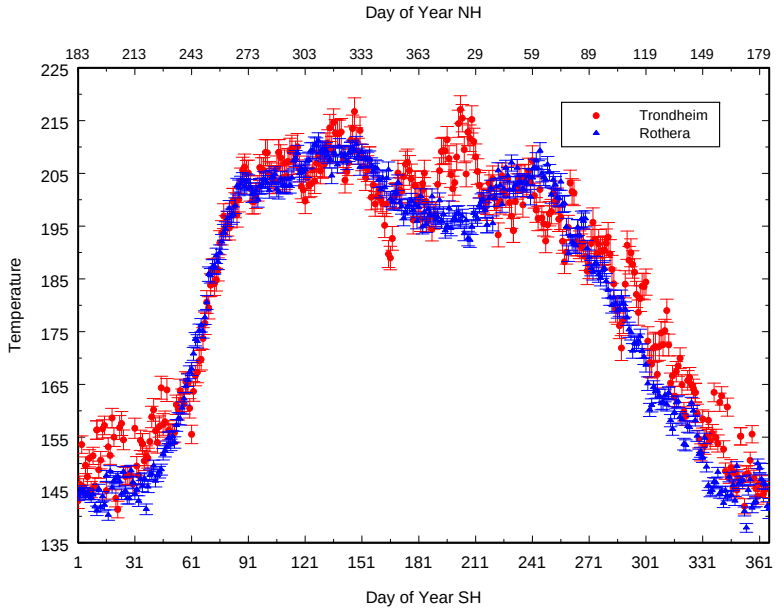

Figure 2.9: The temperature in the mesosphere and lower thermosphere over Trondheim and Rothera, Antarctica. Axis depict days in the northern and southern hemispheres (NH and SH) so that the centre of the figure represents the 1st of January. The figure is from P. Espy, personal communication.

or Lomb-Scargle transform, see section 3.4.1.

Atmospheric gravity waves are the phenomenon of air pressure behaving like internal ocean waves in the atmosphere. Gravity waves are a significant source of energy transfer in the middle atmosphere and drive the pole-to-pole circulation. The waves have a significant impact on spatial and thermal characteristics of the upper atmosphere (Nappo 2013). They are also the reason the middle atmosphere is so far from radiative equilibrium, as stated in section 2.1.

Gravity waves are longitudinal waves, which means that the air movement is parallel to the energy propagation direction. Gravity waves appear due to an initial pressure difference which might be caused by mountains, cities or thunderstorms. Air hitting such obstacles will rise on the windward side and sink on the lee side. Rising air will slow down, and the pressure at the original position will increase. Because of adiabatic expansion, this air will also cool down. The lee side will experience decreasing pressure as air is moved downward and away. This initial pressure disturbance causes a shift in the air. There will be restoring forces trying to correct this initial imbalance; gravity and buoyancy. Gravity

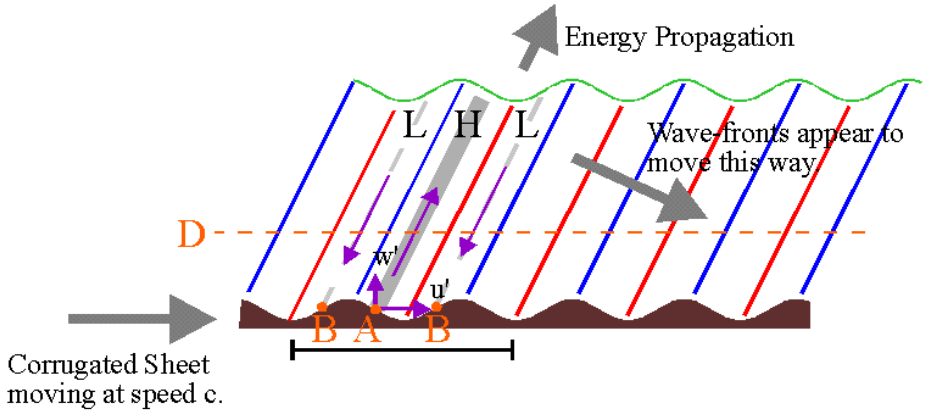

Figure 2.10: An illustration of how a gravity wave behaves. It is visualised through a corrugated sheet moving through a fluid. As the corrugation moves through the air, the air is forced to oscillate and propagate away, and waves are created. The figure is taken from Hocking 2001.

will pull air parcels that are heavier than their surroundings downward. This movement might overshoot, and buoyancy will push the parcel back up. Had the air been stationary, this would have caused an oscillating effect up and down. An initial horizontal movement of the air will cause a cascading effect where air columns are affected by imposing air parcels with higher or lower density. This is illustrated in figure 2.10, where the waves are caused by moving a corrugated surface through a fluid.

The pressure perturbation and its effect as longitudinal waves result in waves with energy propagation parallel to airflow and phase velocity perpendicular to group velocity. A viewer would see a phase front moving downward at one fixed location in time for upward energy propagation. An article from P J Espy and Stegman 2002 presents different transmissions of upward propagating gravity waves in spring and fall at 60°N. This effect might affect the winds over Trondheim.

Chapter 3

Method

Section 3.1, section 3.2, section 3.4.1, and section 3.4.2 are taken from Mohr 2021, a project report laying the ground work for this thesis.

3.1 OH Spectrometer

The spectrometer used for measuring OH intensity in the mesosphere and the lower thermosphere is a Shamrock spectrograph with an iDus InGaAs detector array from Andor. It is located at Dragvoll, NTNU, and measures the intensity of the wavelengths that the OH radiates during nighttime. When the spectrometer is active is automatically determined by the zenith angle of the sun. The following description of the technicalities and workings of the spectrometer is based on (Hennum and P. Espy 2013) and (Berge and P. J. Espy 2011). The parts comprising the spectrometer are listed in table 3.1.

The Shamrock SR-163 has a focal length of 163 mm and a numerical aperture of f/3,6. The wavelength range can be changed with a micrometre drive. The Andor iDus InGaAs camera is a linear PDA detector with a weave length cover of $0.6 - 1.7\,\mu\mathrm{m}$ and a minimum exposure time of $1.4\,\mu\mathrm{s}$. To keep the thermal noise to a minimum, the instrument must be cooled by a built-in thermoelectric element which can cool it down to -90°C, depending on the surrounding temperatures. The operating temperature has been set to -50°C (Hennum and P. Espy 2013). The instrument's response to temperature is non-linear and can be seen in figure 3.1.

The shutter protects the instrument during the day and is used to take background measurements. The spectrometers response to wavelengths are described in (Baker et al. 2001).

Part	Name
Spectrograph	Andor Shamrock SR-163
Camera	Andor iDus InGaAs micro 1.7 DU491A
Shutter	Melles Griot 04 UTS 201
Shutter control	Melles Griot 04 ISC 850
Cooling	Koolance Exos-2
Grating	Andor SR1-GRT-0600
Slit	Andor SR1-ASM-0020

Table 3.1: The different parts that comprise the spectrograph, which measure the OH intensity.

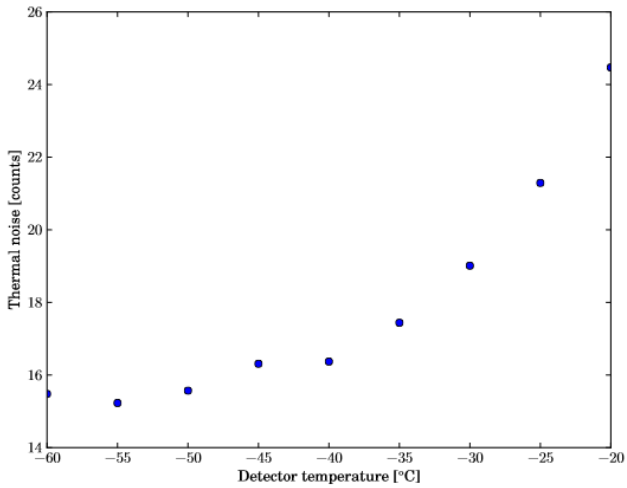

Figure 3.1: The thermal noise in the spectrometer was measured as a standard deviation to the residuals for subsequent background scans as a function of instrument temperatures. Source: (Hennum and P. Espy 2013).

Equation (3.1) gives the channel to wavelength relation,

$$\text{Wavelength } [nm] = -0.86627 \cdot 10^6 \cdot SCN^2 + 0.2071 \cdot SCN + 1333.6, \qquad (3.1)$$

where SCN is the super-channel-number. The SCN ranges from 1-2080, and the (3,1) can be found starting at 625. The resulting wavelength measurements range from 1462.7 - 1672.8nm.

The spectrograph works like a camera. To account for background noise, the detector takes a black snapshot with a closed lens which is refreshed every fifth measurement. It then takes 4-5 measurements of the atmosphere and subtracts the background noise retrieved from the black measurement from the atmospheric measurements. The final result is the average of these measurements. A few seconds later, the camera takes a new black background snapshot and subsequently new intensity measurements and averages. The measurements are a function of wavelength and the nightly average is visualised in figure 2.5.

The spectrometer's response to channel to wavelength has been described in detail in (Berge and P. J. Espy 2011). This was done by using the spectrometer on a source of radiation with known intensity results and comparing the spectrometer's results to the known values. The result is a response curve on the form figure 3.2. The response curve visualises how the measurements in the higher nanometer scale are returned as having lower intensities than they actually have. The spectrometer returns the acceptable intensities up until about 1550nm. At this point, the measured intensities values returned by the spectrometer decrease rapidly compared to the actual intensity.

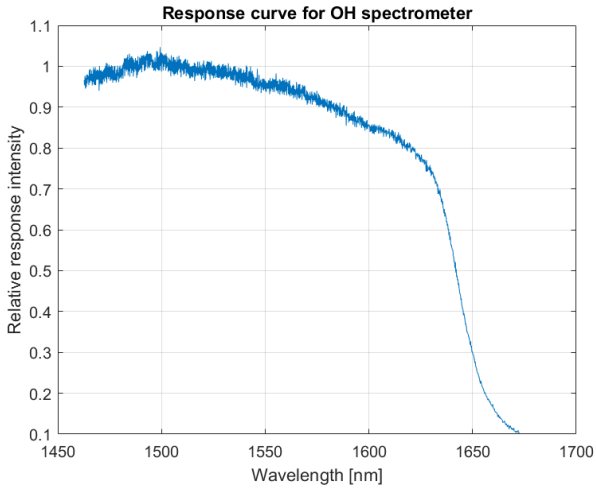

Figure 3.2: The response function in the wavelength region is 1460-1672 nm.

The Andor spectrometer measures the OH intensity during the night. The result is time series of varying lengths, as the time the spectrometer is active depends on the length of the night. For Trondheim, located at 63°N, the length of a night varies from 12h 52min on the 21st of December, with a dark period of 19,5 hours (dark period being the total night and twilight period), to having no natural night time, but 3,5 hours of twilight on midsummer, the 21st of June (*Soloppgang og solnedgang i Trondheim* n.d.).

The spectrometer takes 40-50 measurements an hour. Since the different branches will radiate at different frequencies (section 2.3, section 2.4), the spectrometer will register the intensity of the different wavelengths at which these branches radiate. In addition, the

Sodium intensity (Na) is measured. Integrating over time for the relevant wavelengths makes it possible to isolate the relevant OH branch's intensity throughout the night. Existing data scripts in MATLAB have been used to read and retrieve the relevant data for this project report. Here we use the full intensity spectra containing both the (3,1) and (4,2) lines through the night, as shown in figure 2.5. In addition, the nightly intensity of the (3,1) and (4,2) Q-branches was considered, as they give a good indication of the weather and how the intensities change through the night. To go from figure 2.5 to figure 2.2a, a program in MATLAB integrates under the relevant Q-branch for each time unit, and returns the normalised intensity. The time each measurement is taken is saved along with the intensities for the different radiations. The time is saved as an array from starting hour (e.g. 14,57 = time: 17:34) to final measurement after midnight (e.g. 32,27 = time 08:16).

Since the OH exists in the MLT, the spectrograph's measurements of OH are dependent on the amount of clouds overhead. It is therefore necessary to only look at cloudless days. This was done by looking at the Na-intensity. The Sodium intensity is a reflection of the thickness of the cloud level. This is because the street lamps used in Trondheim are Sodium based lights, which reflect off of the clouds and can be measured by the spectrograph. An OH spectrum of the (3,1) and (4,2) on a clear night can be seen in figure 2.2a, compared to a night with clouds coming in, figure 2.2b. It was discovered that when the sodium intensity passed 50 counts, an anti-correlation between the sodium intensity and the OH intensity took place. By looking for days where the level of Na didn't pass 50 counts per second more than 20 times during a night, it was possible to pick out the clear nights. When talking about the time series of OH and wind, it is understood nights with no clouds.

This thesis considers nightly OH intensity. Since the OH is measured almost every second, it was necessary to average the OH intensity for every hour for comparison with the hourly radar data. In combination with averaging the intensity, the time series also had to be converted to hourly based values. The hourly radar integration is given by the central time of integration, i.e. the half-hour time stamp. To work with compatible data sets, it would be convenient to start the hourly average for OH in a similar fashion. Therefore, the hourly average was used, and the corresponding time stamp was set to the half-hour in the relevant time interval. It was discovered that this time interval retained the general shape of the OH intensity during the night, as seen in figure 3.3.

In addition to the nightly intensities, the intensity spectra on the form figure 2.5 at a 15-minute interval were considered. This process is described in more detail in section 3.3.

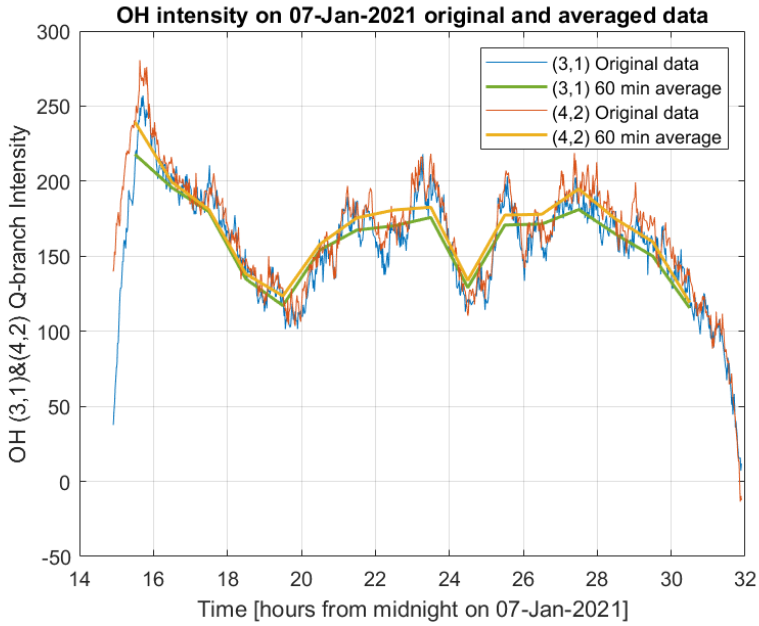

Figure 3.3: Example of the OH intensity and hourly averaged OH intensity for the (3,1) and (4,2) Q-branches. The date measured: January 7-8, 2021.

3.2 SKiMET Meteor Radar

The SKiMET meteor radar uses meteors entering the atmosphere to measure the wind direction and strength in the mesosphere and lower thermosphere. It is located at Dragvoll, NTNU, in Trondheim. With the exception of some downtime due to malfunction, the radar has been operational since 2012. The SKiMET radar consists of 8 transmitting antennas of 1kW and 5 receiving antennas. The sampling frequency is 34,21Mhz at a wavelength of almost 9m. Due to the transmitting antennas' radiation pattern, the radar receives the strongest signal at 20° to 50° from the zenith.

When meteors enter the atmosphere, the high speeds at which they enter, combined with the thickening atmosphere, cause them to leave an ionised plasma trail as they burn up. This ionised dust will exist in the upper atmosphere from 1 to 4 seconds, and in this period, it will drift with the wind. The radar emits a transmission signal, compares the location and phase difference of the signal scattered from the meteor trail affected by the neutral wind, and returns the desired calculations. The radars measure the meteors entering the MLT at the altitudes of 82km, 85km, 88km, 91km, 94km, 98km, 103km and 109km. The frequency of the radar results in a sensitivity to meteors that is roughly Gaussian in shape and centred near 90 km. As a result, there are generally insufficient meteors recorded between 103km and 109km to determine a wind on an hourly basis. However, the radar's

sensitivity curve closely matches the OH intensity versus altitude shown in figure 2.7.

The meteor radar is turned on at all times. It returns an hourly average of the zonal wind, meridional wind and number of meteors used for the calculation. The average number of meteors an hour for all altitudes varies from approximately 100 to more than 500. The meteor runs daily from 00:00 to 23:59, with the timestamps being the central hour of integration.

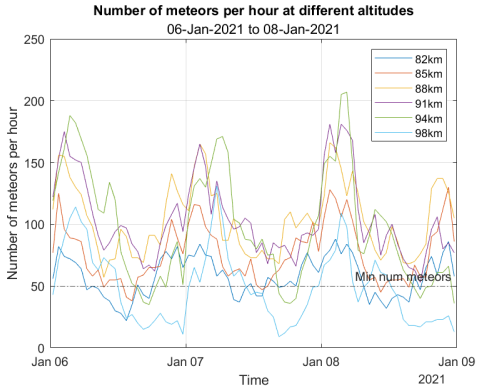

(a) Number of counted meteors per hour per altitude 6.-8.01.2021

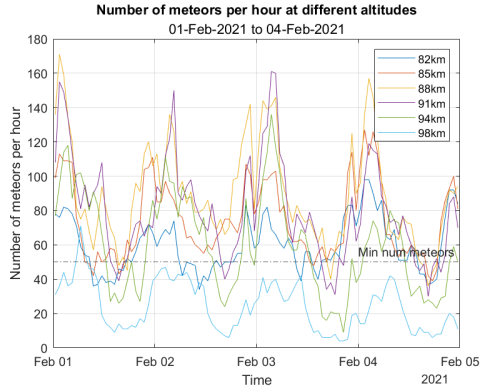

(b) Number of counted meteors per hour per altitude 1.-4.02.2021

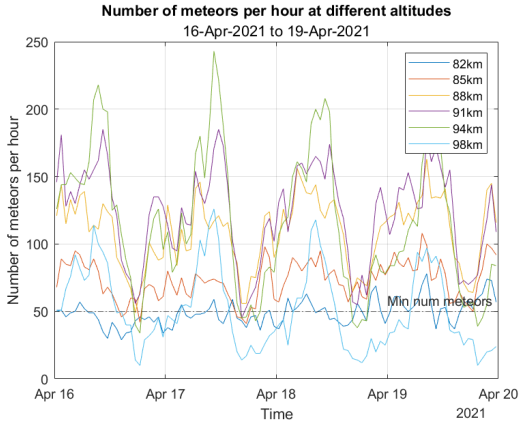

(c) Number of counted meteors per hour per altitude 16.-19.04.2021

Figure 3.4: The number of meteors at different altitudes that were used to calculate the meridional wind at the different altitudes during the periods in January, February and April 2021.

The quality of the wind will depend on the number of meteors entering the atmosphere. On average, about 1000 meteors enter the atmosphere each day. The project of Klemsdal 2015 describes the uncertainty of the average wind measurements depending on the number of meteors. To have wind measurements with an acceptable low error, there must be at least

50 meteors each hour at each altitude to result in a sufficiently good average. The number of meteors counted per hour used in the measuring of the meridional wind at different altitudes can be seen in figure 3.4.

The spectrometer measured the OH intensity in the atmosphere, and the natural OH density distribution follows a Gaussian distribution with a centre at 88km and a half-width of 6-8km (section 2.2). This can be seen in figure 2.8. To compare the wind and OH, the wind has to be weighted by a Gaussian distribution function $W(h)$, which resembles the OH density distribution. This weight function is on the form

$$W(z) = \exp \frac{(z - z_0)^2}{2\sigma^2}, \tag{3.2}$$

where z_0 is the centre peak equal to 88km, and $\sigma = 6$km. This weight function was then used to calculate a weighted total wind, by using the formula

$$w(t) = \frac{\sum_{z=1}^{z=8} W(z)u(z,t)}{\sum_{z=1}^{z=8} W(z)}. \tag{3.3}$$

Here, the values $z = 1...8$ are the 8 different heights ranging from 88km to 109km listed above, $u(z)$ is the wind at height z, and w is the final weighted wind. The weighted wind can be seen with the 6 wind measurements at different altitudes for the meridional wind, in figure 3.5. From here on, the term *wind* will be used for the weighted meridional wind time series.

3.3 Temperature calculations

This section introduces the numerical approach used to calculate the temperatures for the (3,1) and (4,2) Meinel bands. A program written in MATLAB does the basic calculations and may be used as a baseline for further research and temperature calculations. The routine consists of choosing cloud-free days, as described in section 3.1, and evaluating the average intensity spectra for OH at 15-minute intervals. Six Gaussian curves were fitted to the P-branches of the (3,1) band and the P-branches of the (4,2) band for each interval. The resulting fitted Gaussians representing the intensities of the individual rotational lines were then used to evaluate the temperature with data from the HITRAN database. A linear fit to the scaled natural logarithm of the intensities is then applied to the resulting peak calculations using the method described in section 2.5 and equation (2.37).

The following section explains the procedure by which the nightly temperatures were calculated. As described in section 2.5, the temperature is calculated by using the measured OH intensity for the different P-branches for the (3,1) and (4,2) Meinel lines. The OH spectra were split into two series to simplify the numerical process, one containing the

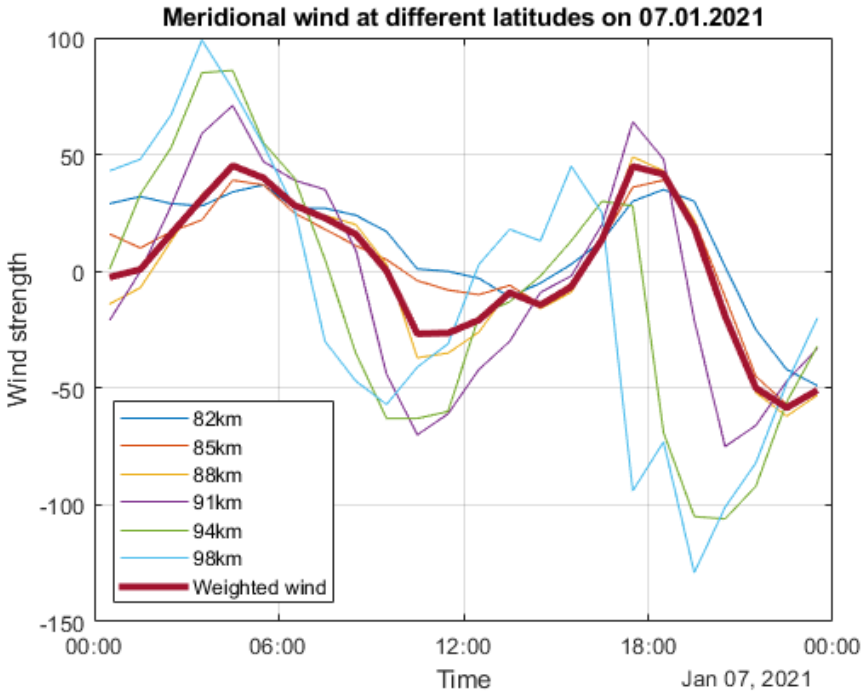

Figure 3.5: The meridional winds at different altitudes with the calculated weighted wind, on 07.01.2021. The wind strength is in meters/second.

wavelength region spanning the (3,1) band, while another containing the (4,2) band. The approach described is the same for the (3,1) and (4,2). The aim was to acquire a temperature calculation at 15-minute intervals through the night. The OH intensity data was read and processed as described above. To acquire 15-minute intervals, the OH spectra were averaged over 15 minutes, and the averaged 15-minute spectrum was used for temperature calculations.

Franzen et al. 2020 presents how a linear temperature fit is a good representation of the temperature up to $J' = 3.5$. For higher rotational levels, a non-linear temperature fit should be used. This thesis uses peaks up to $J' = 5.5$. The error these rotational lines will result in can be seen in figure 3.6 and are deemed to be low enough to warrant using a linear temperature fit.

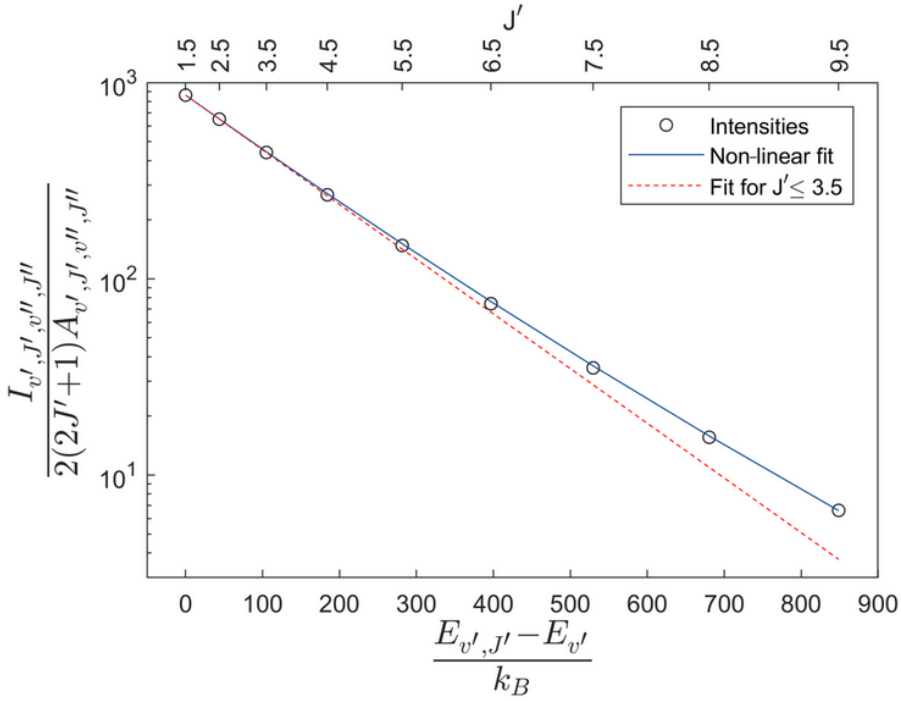

Figure 3.6: Linear vs non-linear temperature fit for different rotational levels (J'). The figure is taken from Franzen et al. 2020.

3.3.1 Deciding on branches

The lines within the P-branches suitable for use are chosen based on the transmission coefficients calculated by P J Espy and Hammond 1995. The high-latitude values during summer and winter and can be seen in table 3.2. The coefficients have to be high during both seasons. The result is that the suitable branches for the (3,1) Meinel lines, these were the lines $P_1(2)$, $P_1(3)$, $P_2(4)$, $P_1(4)$, $P_2(5)$ and $P_1(5)$. For the (4,2) Meinel lines they are $P_1(2)$, $P_2(3)$, $P_1(3)$, $P_2(4)$ and $P_1(4)$.

Line	High-Latitude Summer	High-Latitude Winter
(3,1)		
$P_1(2)$	0.997	0.995
$P_1(3)$	0.976	0.992
$P_1(4)$	0.978	0.994
$P_1(5)$	0.980	0.996
$P_2(2)$	0.959	0.994
$P_2(3)$	0.819	0.970
$P_2(4)$	0.978	0.994
$P_2(5)$	0.978	0.995
(4,2)		
$P_1(2)$	0.970	0.985
$P_1(3)$	0.974	0.992
$P_1(4)$	0.979	0.996
$P_1(5)$	0.972	0.993
$P_2(2)$	0.936	0.985
$P_2(3)$	0.976	0.990
$P_2(4)$	0.979	0.995
$P_2(5)$	0.979	0.996

Table 3.2: The transmission coefficients for the (3,1) and (4,2) Meinel bands, source: (P J Espy and Hammond 1995).

3.3.2 Response function

The region affected by the spectrometer's response curve includes the (4,2) P-branches, as described in section 3.1. The measured intensities are scaled by the response curve for each wavelength to compensate for this. The resulting intensity spectrum can be seen in figure3.7 . This clearly shows how the peaks in the (4,2) region, in reality, have intensities equal to the ones in the (3,1) region. It is relevant to point out that since the (4,2) peaks

are so affected by the calibration, any changes in the spectrometer will significantly affect the measurements of the (4,2) branches. If the spectrometer experienced a temperature change, the results in the (4,2) region would also change drastically. As can be seen in figure 3.1, a slight change in instrument temperature will affect the spectrometer's accuracy, and especially the measurements of the (4,2) region. However, since the calibration error in the (4,2) region is constant, the result is a stable error for the (4,2) measurements. This makes the (4,2) peaks suitable for analysis' such as anomaly detection. Compared to the (3,1) region, which is more exposed to water vapour or Rayleigh scattering (due to its wavelength region), the (4,2) region is more stable. Therefore, it will be used to some degree in this thesis, but with the knowledge that there may be a systematic bias in the absolute temperature values.

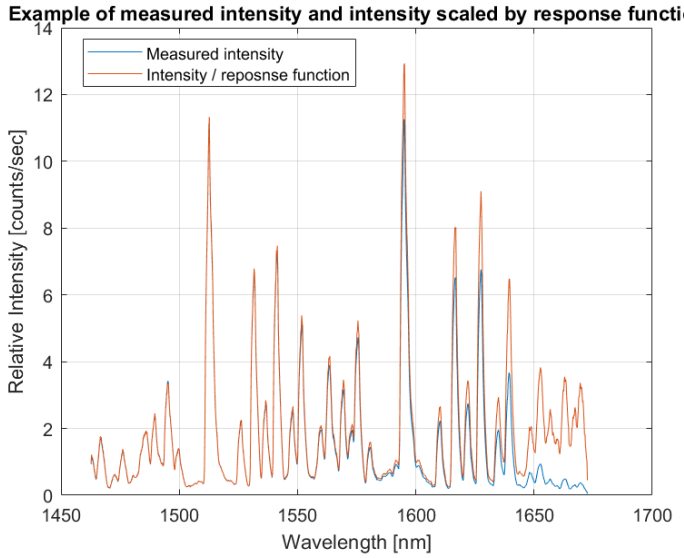

Figure 3.7: Averaged nightly OH intensity spectrum where blue is the measured intensity recorded by the spectrometer, while orange is the actual intensity when corrected by the spectrometer's response function.

3.3.3 Removing the baseline

As Endre Hennum explored in his thesis (Hennum and P. Espy 2013), the shape of an intensity peak around a Meinel line can be seen as a shifted Gaussian. He also pointed out that a baseline could be fitted along the intensity signal's null-points, the minimums of the signal where there should be no radiation measured. The baseline is removed on the assumption that there is a constant amount of blackbody radiation, scattered light and a possible offset due to the dark signal of the spectrometer. By approximating this baseline using a polynomial fitted line and subtracting this from the signal, some noise would be

filtered out of the original signal. Hennum discovered that the (3,1) Meinel lines followed a third-degree polynomial, while the (4,2) baselines better fitted a first-degree polynomial. The null-points were identified by localising the areas between OH lines and assuming any intensity there to be caused by background radiation. For the (3,1) lines, the null-points chosen were between the peaks of $P_2(2)$ and $P_1(2)$, $P_1(3)$ and $P_2(4)$, $P_1(4)$ and $P_2(5)$, and between $P_1(5)$ and $P_2(6)$. These points and the third-degree polynomial fitted through them can be seen in figure 3.8a. For the (4,2) lines, these points were between $P_2(3)$ and $P_1(3)$, $P_1(4)$ and $P_2(5)$, and between $P_1(5)$ and $P_2(6)$. These null-points and the first-degree polynomial can be seen in figure 3.9a. By fitting the appropriate polynomials and subtracting from the original signal, the signals were flattened out so that the no-signal points fell on zero-intensity. This can be seen in figure 3.8b and figure 3.9b.

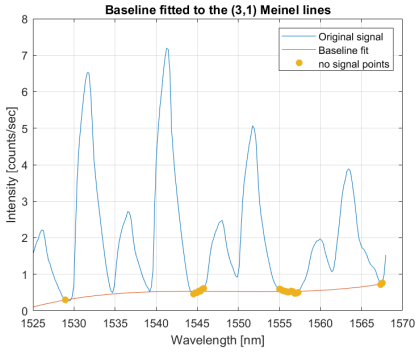

(a) The null-points that were used to approximate the baseline, and baseline.

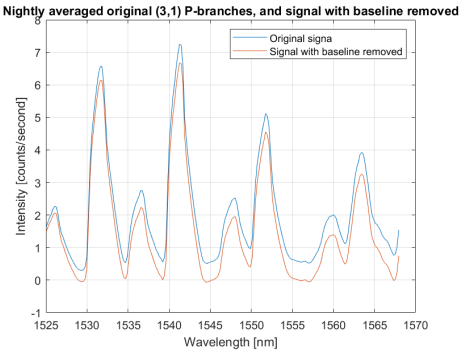

(b) Final signal after baseline removal.

Figure 3.8: The null-points being used in the (3,1) Meinel lines, the fitted 3rd polynomial to these lines, and the final signal after baseline was subtracted from the original signal.

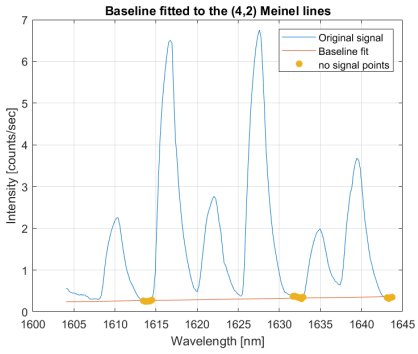

(a) The null-points that were used to approximate the baseline, and baseline.

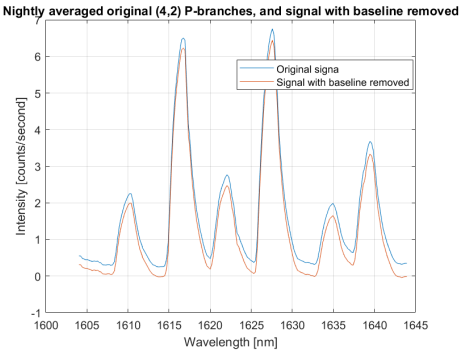

(b) Final signal after baseline removal.

Figure 3.9: The null-points being used in the (4,2) Meinel lines, the fitted 1st polynomial to these lines, and the final signal after baseline was subtracted from the original signal.

3.3.4 Gaussian fitting

Computational routine

A Gaussian can be expressed as

$$g(x) = Aexp[\frac{-(x-\mu)^2}{w^2\sigma^2}]. \tag{3.4}$$

A is the amplitude, x is the evaluated wavelength, μ is the wavelength at the maximum value of a P-branch line, σ is the spectrometer's maximum spectral line width, and w is the scaling factor for the line width which can vary with wavelength. This thesis uses a MATLAB program that has as input the number of Gaussians to be calculated, the mean value μ, and the width σ. The number of Gaussians is the number of peaks evaluated in the (3,1) and (4,2) regions. The program fits Gaussians to the signal at wavelength x by fitting different amplitudes and weights in a least-squares sense. The program runs 10000 fitting routines and chooses the Gaussian wave with the best fit to the signal. The sum of Gaussians centred at the P-branch line positions was fitted to the (3,1) and (4,2) bands, separately.

The spectrometer's line shape is approximated as a Gaussian according to equation (3.4). This was done in MATLAB with a program from Image Analyst n.d. Each line position μ is set at the wavelength of the maximum of each spectral line, and the maximum intensity is used as the initial amplitude, A. σ was set to the largest full-width at half maximum of the lines divided by four. The initial line width correction, w, was set to one. These values were used in a non-linear least-squares fitting routine, using the MATLAB optimisation function *fminsearch()*. A sum of the Gaussians centred at the desired P-branch lines were then least-squares fitted to the data as a function of wavelength over the relevant P-branch regions, as shown in figure 3.10. This procedure was performed separately for the (3,1) and (4,2) bands.

Due to the nature of the program and a varying degree of noise in the signal, the final Gaussian did not always include the desired P-branches. To ensure that the final fitted Gaussian had the necessary intensity information, conditions relating to the number of peaks present and the accuracy of the fit at the maximum and minimums values were put in place. In addition to this, the fitting routine described above was implemented twice. After a first iteration resulting in a fitted Gaussian was conducted, this Gaussian was subtracted from the original signal. The residual was then fitted with a Gaussian, and this residual fitting was subtracted from the original signal. The new signal contained less noise. This signal was used to fit a Gaussian wave in the described procedure, resulting in a better fit as seen in figure 3.10.

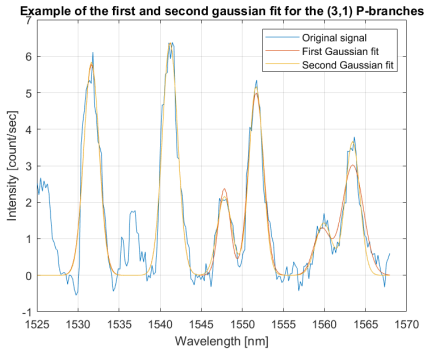

(a) The first and second Gaussian fit for the P-branches in the (3,1) Meinel lines

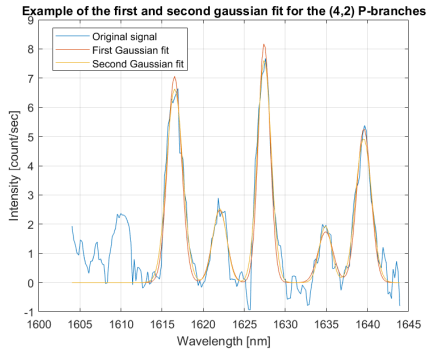

(b) The first and second Gaussian fit for the P-branches in the (4,2) Meinel lines

Figure 3.10: The Gaussian fits the P-branches for the (3,1) and (4,2) Meinel lines. The first fit is a Gaussian fit to the original signal, while the second fit is a fit to the original signal with the residual of the first Gaussian subtracted from it. This example also shows the level of noise present in a 15 minute average of the OH intensity spectrum.

Errors in the Gaussian fits

To evaluate the fit of the Gaussians, the relative root mean square error (RMSE) was used. The RMSE is a measurement of how far out the residuals are and can be mathematically expressed as

$$RMSE(t) = \sqrt{\frac{\overline{(y(t) - \hat{y}(t))^2}}{N}}. \tag{3.5}$$

y is the original signal, $\hat{y}$ is the Gaussian fit, and the overline represents the mean value of the difference between those two signals. N is the number of points in y and $\hat{y}$. The value t represents which time interval the error was calculated for, as this was done on every 15-minute average OH intensity spectra through the night. The RMSE was calculated after the first Gaussian fit (RMSE_1) and after the second Gaussian fit when the residual had been subtracted from the original signal (RMSE_2). An example of the errors for the (3,1) and (4,2) bands can be seen in figure 3.11.

3.3.5 Temperature calculations

The temperature calculations were done by following the theory described in section 2.5. A 1st-degree polynomial was fitted through the calculated values for each relevant P-branch. For each 15 minute intervals, a slope was fitted, and the negative inverse slope number was the average temperature for that Meinel band at that 15-minute interval. The

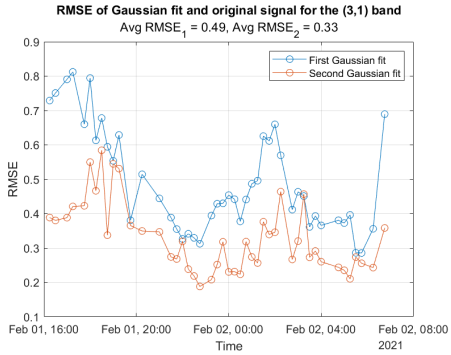

(a) The RMSE for the (3,1) band for the first and second Gaussian fits.

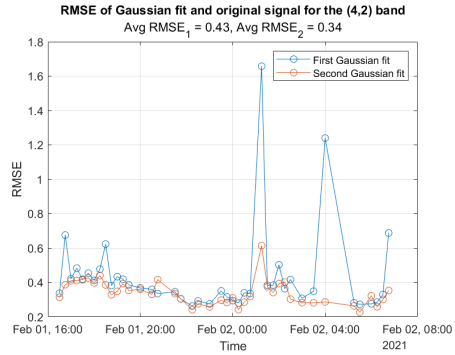

(b) The RMSE for the (4,2) Meinel band for the first and second Gaussian fit.

Figure 3.11: The RMSE for each 15-minute interval on the night 1st-2nd of February 2021. It is visualised for the first Gaussian fit of the original signal, and after the residuals were subtracted and the Gaussian was fitted to the smoother signal.

measured intensity was calculated using the normalised integral for the relevant peak.

As can be seen in figure 3.11, the Gaussian fits did not always converge accurately. One incorrectly fitted line in the P-branch will result in a significant error in the fitted temperature due to the logarithmic relation between temperature and line intensities.

To sidestep this problem, the temperatures that exceeded two times the standard deviation from the median value of the calculated temperature were excluded. The median was used instead of the mean value, as it is less affected by the extreme temperature resulting from the incorrectly fitted line. This procedure was repeated until no values were further than one standard deviation from the median value. The final result was temperatures at points in time where the Gaussian fit was good enough to result in a decent fitted slope and subsequently decently good temperature calculation.

3.4 Data analysis

3.4.1 Frequency analysis: The Lomb-Scargle transform

Lomb-Scargle periodogram is a spectral analysis tool used in signal processing to analyse the frequencies a given signal oscillates at. Similarly to the Fourier transform, it uses the least squares fit of sinusoidal waves to the data to determine the frequency spectra. However, unlike the Fourier transform, which demands evenly spaced data points as input, the Lomb-Scargle transform does not require even measurement intervals. As the OH is sampled at night only, it becomes necessary to use the Lomb-Scargle periodogram instead

of the more known Fourier transform. The result is the same, a frequency spectra. Since this thesis mainly considers atmospheric tides and periods, the frequency will be converted to period by the relation $T = 1/f$. T is the period and will, through this thesis, have the unit hours. f is the frequency.

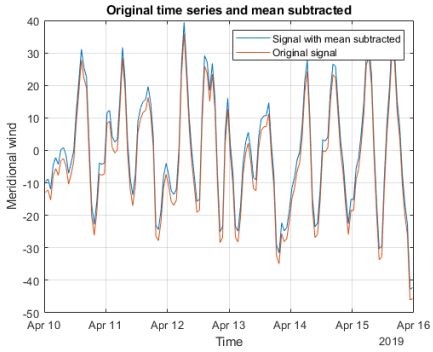

(a) The original meridional wind series and with the mean subtracted.

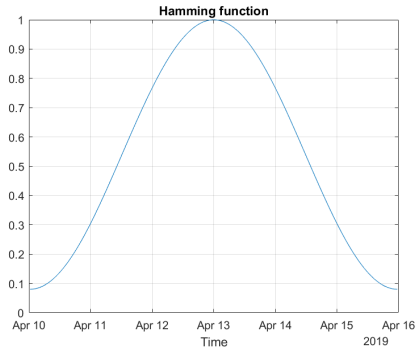

(b) Hamming function.

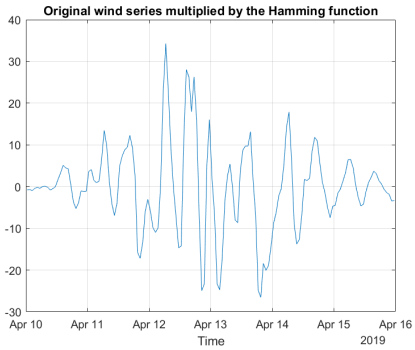

(c) The wind series is multiplied by the Hamming function.

Figure 3.12: The necessary manipulation of the wind time series before L-S transforms for the 10th-15th of April 2019.

The wind is measured continuously, and can be combined into a continuous time series over many days. The OH data is combined into a time series over several days, but where the data points are only sampled at night. During the day, when there are no measurements, there is no data sampled. Since the temperature is calculated using the OH intensity (section 2.5), the same procedure will apply for a temperature time series.

The signal subjected to a frequency analysis is manipulated to simplify the transform. First, the mean is subtracted from the data, bringing the average signal close to zero. The time series is then multiplied by a window function, in this case, the Hamming function. The Lomb-Scargle transform expands the signal to infinity by running the signal in an infinite loop along the time axis. By multiplying the signal with a window function, the

first and last data points are set close to zero, making the transition to a new signal addition almost seamless. The window function minimises the edges of the signal while retaining the general shape. The procedure exemplified with the meridional wind time series can be seen in figure 3.12. The signal is then padded with zeros until the size of the signal reaches the length of the original signal, squared. This does not affect the resolution of the frequency transform but provides a sufficient number of frequencies to be evaluated in the transform to ensure a smooth spectrum.

The script used to calculate the Lomb-Scargle transform also includes an α-value set to $\alpha = 0.95$. This value represents only a 5% chance of peaks reaching this height not being made by random noise and can therefore be considered significant.

3.4.2 Sine waves

Frequencies can be used to represent data by sine waves on the form

$$y(x,t) = A\sin(kx - \omega t + \phi). \tag{3.6}$$

Here, $y(x,t)$ is the resulting wave, A is the amplitude, k is the wave vector, ω is the angular frequency, ϕ is the phase shift, and x and t is the position and time. Since the calculations occur at a fixed position (wavelengths), the kx term is dropped. The angular frequency is measured per day, which means that the diurnal, semi-diurnal and terdiurnal tides will have frequency values of $\omega_{24} = 24/24$, $\omega_{12} = 12/24$ and $\omega_8 = 8/24$. This will be similar to other periods found through frequency analysis.

Chapter 4

Results and discussion

4.1 Temperatures in the MLT

As described in section 2.5 and section 3.3, one can calculate the temperature as long as there exists a clear OH spectrum. In other words, for every cloudless night, the atmospheric temperature in the (3,1) and (4,2) regions can be calculated.

The days and dates used in this thesis will be 06.01.21-08.01.21, 01.02.21-04.02.21, and 16.04.21-19.04.21. These periods are chosen because they consist of long nights or many successive cloudless nights.

Dates	Number of nights	Number of hours of OH sampling	Total number of hours
6.-8. Jan 2021	2 nights	16 hrs	32 hrs
1.-4. Feb 2021	3 nights	14 hrs	42 hrs
16.-19. Apr 2021	3 nights	7 hrs	21 hrs

Table 4.1: The dates, number of nights used, and the average nightly sampling time available where OH radiation was measured. The total number of hours used when considering a time series based on consecutive nights of data is also included.

4.1.1 Nightly temperature calculations

The calculated temperatures are presented as nightly time series with 15-minute intervals and hourly averages. The nightly averages are also given to compare the results with previous studies (Hennum and P. Espy 2013, Berge and P. J. Espy 2011, P. J. Espy et al. 2003).

When looking at the nightly temperatures, it is noticeable that some time series have missing data points. This is due to the procedure explained in section 3.3, where extreme and unrealistic temperatures were excluded from the final temperature series.

	(3,1)			(4,2)		
	T [K]	$\pm$ T [K]	$RMSE_2$	T [K]	$\pm$ T [K]	$RMSE_2$
Date						
6.-7. Jan 21	192.99	9.96	0.44	178.50	7.06	0.42
7.-8. Jan 21	194.22	10.13	0.41	173.28	8.47	0.40
1.-2. Feb 21	194.03	13.30	0.33	175.57	8.72	0.34
2.-3. Feb 21	173.19	8.13	0.30	165.63	10.72	0.36
3.-4. Feb 21	198.71	7.18	0.54	168.01	8.20	0.56
16.-17. Apr 21	164.29	15.32	0.53	155.73	7.09	0.41
17.-18. Apr 21	174.49	9.98	0.45	162.84	7.21	0.47
18.-19. Apr 21	128.36	29.55	0.65	158.63	5.89	0.38

Table 4.2: The nightly average temperature T, the error in the nightly temperature $\pm$ T, and the RMSE error of the second Gaussian fit, $RMSE_2$, for the (3,1) and (4,2) Meinel lines.

Table 4.2 presents the average nightly temperatures for the (3,1) and (4,2) bands, as well as the standard deviation in the nightly temperatures and the relative root mean square errors for the second Gaussian fits that night. Generally, the temperatures for the (3,1) bands are higher than for the (4,2). This is in accordance with temperatures calculated by Hennum and P. Espy 2013. It is also realistic, as the (3,1) density is found at a lower altitude than the (4,2) density, at which point the temperature is higher, figure 2.8. In addition, comparing with temperatures in the mesosphere and lower thermosphere applied by P. Espy in figure 2.9, the average temperatures presented here seem appropriate. The (3,1) temperature calculated for the 19th of April can be said to be incorrect. The (3,1) temperature is low, and the root mean square error is high. It is included as the (4,2) temperature can be used. Not included here are days in April following the 19th of April 2021. These days

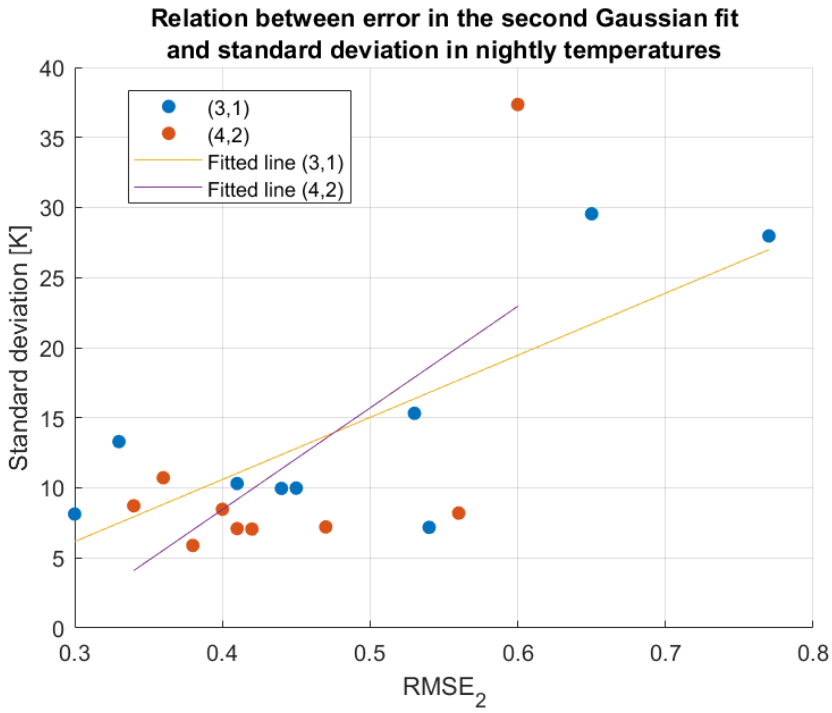

Figure 4.1: A linear fit to the relation between the standard deviation and relative RMSE in the second Gaussian fits for the (3,1) and (4,2) average nightly temperatures presented in table 4.2. If the $RMSE_2$ is greater than 0.55, there is most likely a problem with the fitting of the Gaussians.

consisted of extremely unrealistic temperatures around 40K. A closer inspection of the 15-minute average OH intensity spectra showed that the program in MATLAB was unable to apply sufficiently good fits to the spectra. In addition, the spectrometer is vulnerable to small temperature changes or other external factors affecting the instrument. Such changes would, as described in section 3.3, affect the (4,2) temperatures to a large extent. It is also important to remember that these numbers are averages and that nightly weather changes will affect the results.

It is interesting to note the relation between the standard deviation in the temperatures and the second Gaussian fit error. This is presented in figure 4.1. This can be understood as as long as the $RMSE_2$ is below approximately 0.55, natural causes can cause the standard deviation in the temperature. If the $RMSE_2$ reaches above this limit, the variation in the temperature is likely due to a bad fitting of the Gaussian waves, which resulted in a possible incorrect temperature fit. We can use this observation to comment on the reliability of the data used to calculate the temperatures.

One night is attached in figure 4.2 from each period mentioned earlier, to take a closer look at the nightly temperatures and their behaviours. As can be seen, when considering

the 15-minute intervals, it is clear that the temperatures vary a lot over a short period of time. This variation might be due to errors or differences in the Gaussian fits, affecting the measured intensity and subsequent temperature slope fit. However, the rapid temperature changes are in accordance with similar results presented by Mulligan et al. 1995, which also shows relatively large temperature variations for each calculation, for the (3,1) Meinel band. In addition, other wave motions affect the OH, with gravity waves being a notable factor. These waves have periods shorter than one day, typically in the range between 5 minutes to a couple of hours, with most occurring at about 20 minutes to an hour (Fritts and Alexander 2003).

The hourly trend is shown in orange for both Meinel bands. These calculations are included to make the temperatures compatible with the meridional wind and show more stable temperature changes through the night. Even though it is more stable than the 15 minute interval time series, it still varies a lot through the night compared to the meridional wind (figure 3.5) and the hourly averaged OH intensity (figure 3.3). When considering the tides in the temperature, it is important to consider how much the 15-minute interval temperature changes as opposed to the hourly interval. When conducting a Lomb-Scargle transform, it will be better to use the hourly averages to avoid having to analyse a periodogram that depicts all the small oscillation periods making up the nightly temperature. Effects caused by for example gravity waves (Fritts and Alexander 2003) would be dampened by the use of the hourly temperature average.

4.1.2 Tides in the temperature

A LS-transform for the periods in January-21, February-21 and April-21 have been done for times series consisting of temperatures with 15-minute intervals and hourly intervals, seen in figure 4.3. When comparing the Lomb-Scargle transform of the different time series, it is noticeable that the longer the time series is, the better the transform is. This can be seen by considering the peaks reaching the 95% level. This line indicates the amplitude a peak must have to be considered significant and not likely to be a product of noise in the signal. Interestingly enough, the temperature series in February (figure 4.3e, figure 4.3f) is the only one where both the (3,1) and (4,2) temperature peaks reach the 95% confidence level. This is also the longest time series (in number of hours included) out of the three periods, table 4.1. The transforms of the 60-minute intervals include fewer shorter periods than the 15-minute intervals. The close correspondence between the (3,1) transform and the (4,2) transform indicates similar tides in the two temperature series.

It is difficult to divide between what is short period peaks caused by gravity waves (Fritts and Alexander 2003) and what is statistical noise. Geophysical noise would be the shorter periods in the temperature resulting from natural OH variations caused by gravity waves. If these shorter periods have a high amplitude, they might obscure the longer periods entirely. On the other hand, statistical noise is a result of inaccurate OH measurements caused by instrument errors and bad temperature fittings. This will lead to more uncertainty and higher variability in the data and might affect the nightly temperatures when combined in

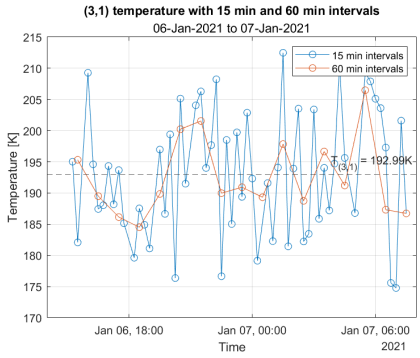

(a) Temperature for the (3,1) Meinel band in January.

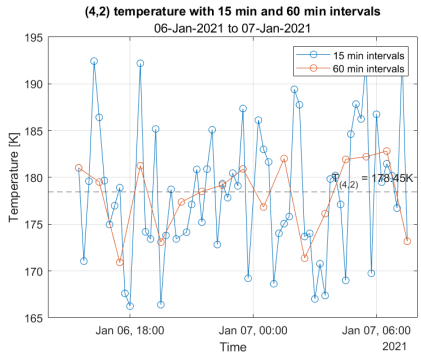

(b) Temperature for the (4,2) Meinel band in January.

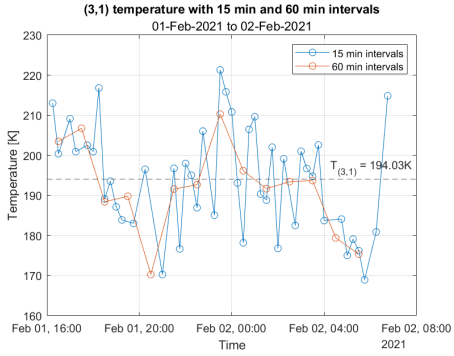

(c) Temperature for the (3,1) Meinel band in February.

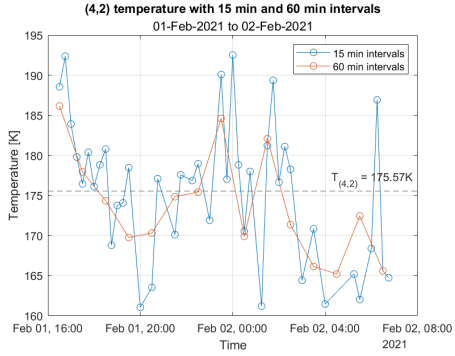

(d) Temperature for the (4,2) Meinel band in February.

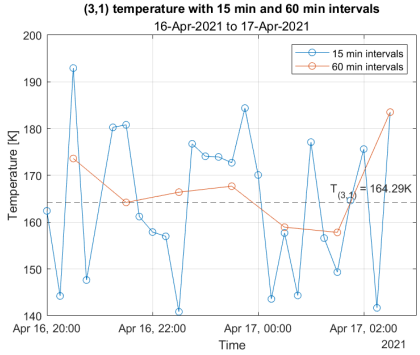

(e) Temperature for the (3,1) Meinel band in April.

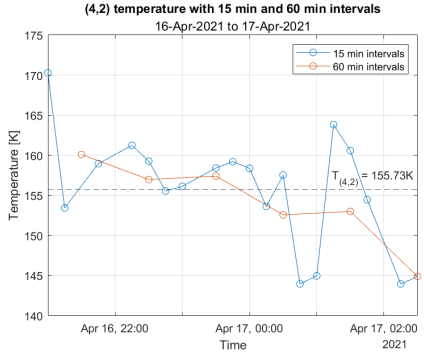

(f) Temperature for the (4,2) Meinel band in April.

Figure 4.2: Nightly temperatures for the (3,1) and (4,2) Meinel bands from one night in January, February, and April. The temperatures are presented as they are calculated, with 15-minute intervals, and with the hourly averages.

a time series and used in a frequency analysis.

The LS transform behaves differently, not only considering geophysical and statistical noise but also regarding the tides it returns. This brings up how the sampling time, length of night, and number of days used in the time series affect the results. Since the temperatures consist of limited time series only present when the OH is sampled, how does the sampling time affect the ability to derive tides from the data?

4.2 Viability of using non-continuous time series to derive tides

A combination of pure sine waves and the meridional wind time series has been used to investigate how the sampling time affects the tides returned through a frequency analysis. Since the wind has data creating a continuous time series as long as the meteor radar is functioning, getting a power spectrum with well-defined peaks representing the tides in the wind at that time is easy. This was done in the project report, Mohr 2021. Creating a new time series with wind data only present at the times the OH was sampled makes it possible to analyse how a Lomb-Scargle transform of the original continuous time series compares with an LS-transform of the wind at sampled OH time stamps. From here on, a time series consisting of data only when the OH has been sampled shall be denoted a sampled time series, or a sampled wave. The original time series will be called a continuous time series. There are no OH intensity requirements, meaning that all days of sampled OH can be used.

4.2.1 Sampling effect on sine waves

To evaluate the impact of the sampling effect and what the sample time has to say about the period spectra produced, simple sine waves with periods of 8 hours, 12 hours and 24 hours were analysed. These periods were chosen as they are found in the meridional wind as the terdiurnal tide, semidiurnal tide, and the diurnal tide. In Mohr 2021 they were also found to be present in the OH intensity. A power spectrum of a sine wave with the above mentioned periods spanning over 5 consecutive days, and one including just the timestamps where the OH has been sampled, were evaluated through the LS transform. The measurements used were from January 2021. The power spectres for the two waves can be seen in figure 4.4.

For the sampled wave, the 8 hour period, 12 hour period, and 24 hour period were present to some degree at all times, (figure 4.4a, figure 4.4b, figure 4.4c). These periods had a higher signal to noise ratio, as they didn't reach the 95% confidence level. The continuous sine wave depicted only the original period in the power spectra output. The inputted frequency was always the dominating one in the spectra, and reached the 95% confidence level at all spectra. The fact that the OH was sampled periodically at night might explain

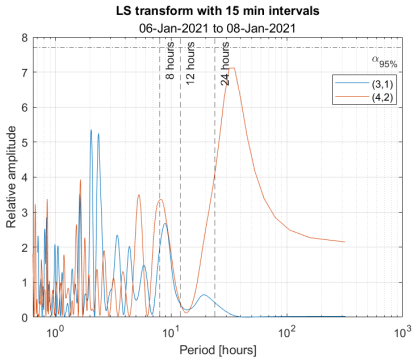

(a) The LS-transform of the temperature in January, with 15 minute intervals.

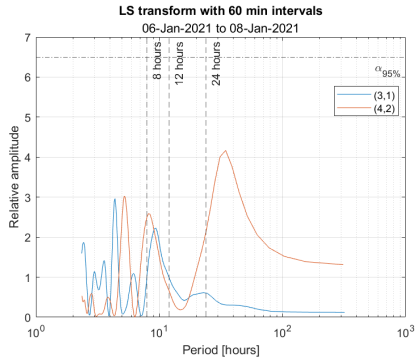

(b) The LS-transform of the temperature in January, with 60 minute intervals.

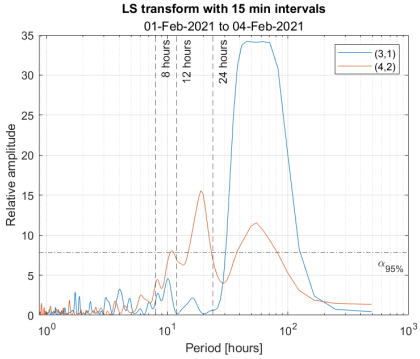

(c) The LS-transform of the temperature in February, with 15 minute intervals.

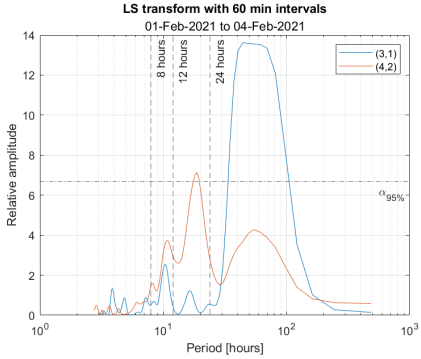

(d) The LS-transform of the temperature in February, with 60 minute intervals.

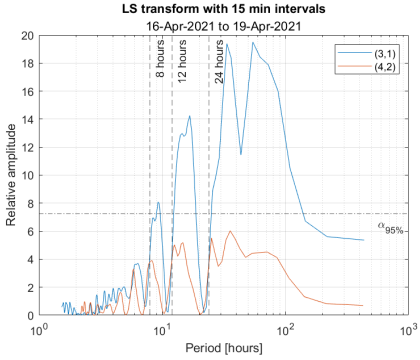

(e) The LS-transform of the temperature in April, with 15 minute intervals.

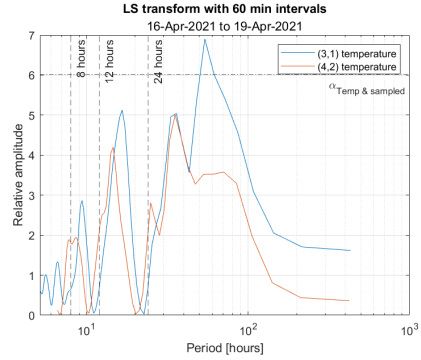

(f) The LS-transform of the temperature in April, with 60 minute intervals.

Figure 4.3: Lomb-Scargle transforms of (3,1) and (4,2) temperature time series during the dates presented in table 4.1. The time series on the left side are with 15 minute intervals, and on the right side hourly intervals is used. Examples of nightly temperature behaviour can be seen in figure 4.2

the presence of the 12 hour and 24 hour tide.

The superpositioned LS transformed wave is also visualised in figure 4.4d. The blue curve shows the continuous signal and the three peaks equally represented, while the orange signal is the sampled signal. This clearly shows how sampling a signal affects the periods present and the signal to noise ratio.

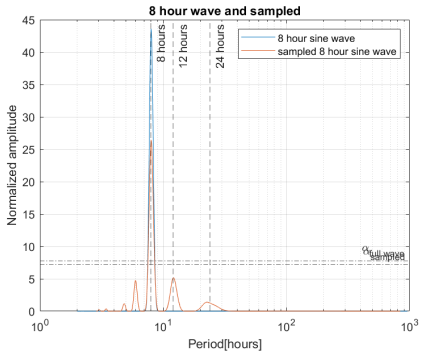

(a) Sine wave with a period of 8 hours, the continuous signal and at sampled times.

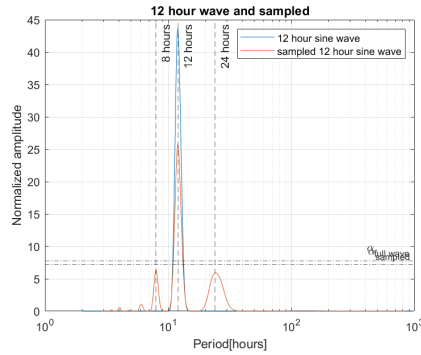

(b) Sine wave with a period of 12 hours, the continuous signal and at sampled times.

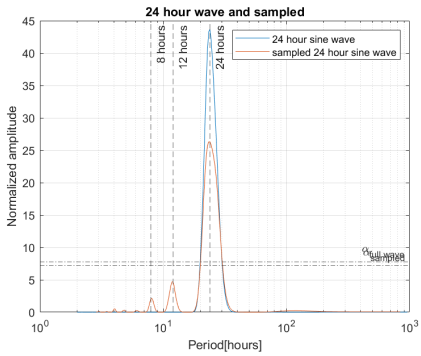

(c) Sine wave with a period of 24 hours, the continuous signal and at sampled times.

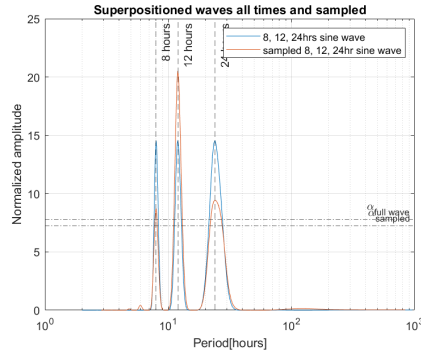

(d) Superpositioned sine wave with a period of 8hrs, 12hrs and 24hrs, the continuous signal and at sampled times.

Figure 4.4: The Lomb-Scargle transformed sine waves with different periods. The length of the full sine wave is equal to the length of the meridional wind series over five days, while the sampled signal is present when the OH was sampled those four nights in between.

These results show how sampling will produce artificial tides in a periodogram. In addition to new periods, some noise will also appear.

4.2.2 Sampling effect on meridional wind

The sine waves used to produce figure 4.4 were made based on five days of data from January 2021. The sine waves used are noise-free, returning clear results. To compare how the meridional wind behaves, the measured meridional wind is used in the same way as described above. Hibbins et al. 2007 describes how different tides dominate the meridional wind at different times of the year. By using similar dates as above, the beginning of January, we should be expected to get a dominating 12-hour tide in the periodogram, as the semi-diurnal tide is the dominating tide during winter in Norway (Hibbins et al. 2007). The power spectrum can be seen in figure 4.5a, and can be compared with the LS transform in figure 4.4b. The continuous wave presents a clear 12 hour period, while the sampled meridional wind includes the 8 hour and 24 hour period. The only thing differentiating the two power spectra is that there is some noise in the meridional wind causing some noise (geophysical or statistical) in the power spectra.

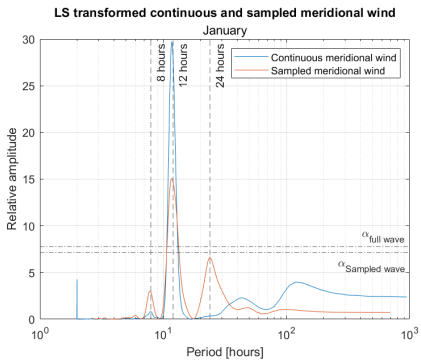

(a) The meridional wind in January LS-transformed as a continuous time series, and as a time series only consisting of wind data at sampled OH times.

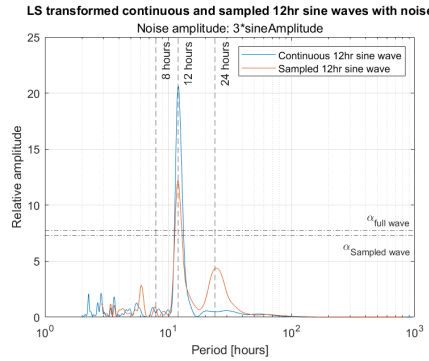

(b) Periodogram of a 12 hour continuous sine wave, and one sampled at the OH measurements. The sine wave has been added uniform random noise with an amplitude of 3 times the sine wave amplitude.

Figure 4.5: Power spectrum from the measured meridional wind and a spectrum from a similarly simulated case where sine waves with noise are used.

This kind of noise can be simulated in the sine waves transform by trial and error. By adding noise to a sine wave with a period of 12 hours and doing a frequency analysis of the continuous and sampled wave, it is possible to see the similar behaviour as in figure 4.5a. This can be seen in figure 4.5b. The more noise is added, the more noise is visible on the far left side of the periodogram, and the greater the big period batch on the right side becomes.

An analysis of the meridional wind at sampled times and as a continuous signal was done. By calculating the correlation coefficient between the LS-transform of the continuous meridional wind and the sampled meridional wind, it was possible to get a condition for when the sampled wind was able to provide tides that were in accordance with the tides returned by the continuous wave. Figure 4.6 shows how the sampled transform matches

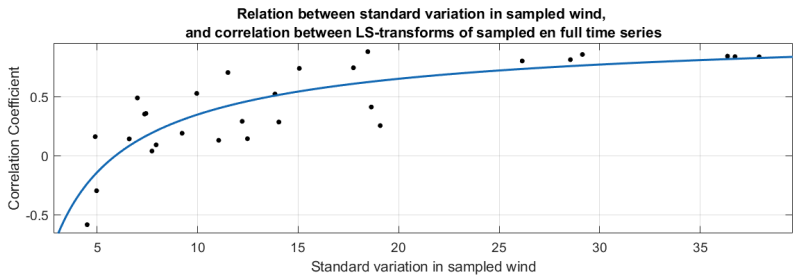

Figure 4.6: Relation between standard deviation in the sampled wind and the correlation between the LS transform of the sampled wind series and the full wind series.

the continuous LS-transform when only one night is evaluated through an LS-transform. The correlation coefficients are plotted against the standard deviation in the sampled wind, and the plot fits a power function. This shows that if the standard deviation in the sampled wind is above 20, the sampled wind can be a good represenation of the continuous time series. This makes sense as more variation in a limited wave makes it easier to isolate the correct tides.

These results show how sampling a wave at night will affect the derivation of tides. In a frequency analysis, a non-continuous time series will return more than the significant tide. Therefore, it can be assumed that the OH intensity and the temperature power spectrum are also subject to this phenomenon. The challenge then becomes distinguishing between the actual tides in the data and artificial tides due to the sampling effect. Knowing this effect makes it possible to compare the LS-transform of sampled series such as OH and temperature with the sampled series of meridional wind at the same instances. One can then compare the transform of the sampled meridional wind to the power spectrum of the continuous meridional wind to determine the tide.

To investigate this further, it is relevant to look at how the power spectrum of the meridional wind and the sampled meridional wind appears if one only considers one night. The dominating tide is known as the semi-diurnal tide by keeping with data gathered in January. Figure 4.7a shows how the meridional wind LS-transform in January is for a 24-hour long wave and for a wave sampled at night lasting 14 hours. As can be seen in figure 4.7a, the spectrum appears slightly shifted when considering only the nightly time series values of the wind. By comparing it with a sine wave of similar length, it is clear that the meridional wind this night barely contained any geophysical or statistical noise, figure 4.7.

Interestingly enough, when comparing the wind spectrum analysis to the Lomb-Scargle transform of the temperature simultaneously, it appears that the temperature spectrum is shifted in the same fashion as the limited wind spectrum. This can be seen in figure 4.8a. Figure 4.8a shows how the Lomb-Scargle transform of the (3,1) and (4,2) rotational temperature compares with the Lomb-Scargle transform of the continuous and sampled meridional wind. Using the sampled meridional wind spectrum as a signature of the semi-diurnal tide, one can argue that since the temperature transforms keep a shape and centre similar

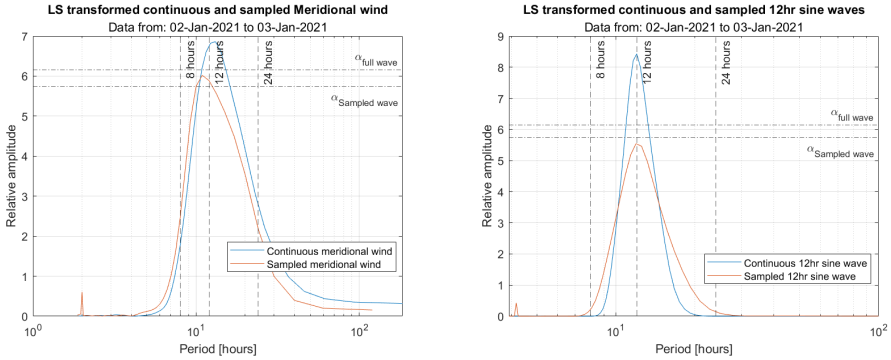

(a) Meridional wind over 24 hours, and data only during sampled OH time.

(b) Sine wave with a period of 12 hours, the continuous signal and at sampled wave.

Figure 4.7: The Lomb-Scargle transform of the Meridional wind on the night between the 2nd and 3rd of January 2021. The cross-spectrum analysis uses 24 hours of data and only 14 hours during which the OH is present and measured. α_{24h} is the 95% confidence level for the time series with 24 hours of data, and similarly for the α_{12h}.

to the sampled meridional wind, the temperatures have a tide of 12 hours this night.

However, this is not always the case. When evaluating two subsequent nights in January, the temperature transform matches the sampled wind transform on only one of the nights, figure 4.8. This does not mean that the method mentioned above can not be used. It means that the temperatures on the night where the power spectrum does not match the sampled wind, do not have tides in common with the wind. By elaborating on this work and gathering more examples of how a sampled time series power spectrum would look compared to the continuous time series power spectrum, it might be possible to create a database with shapes that depend on the length of sampled time and number of days. This could then be used to characterise the temperature and OH tides that are affected by the sampling effect.

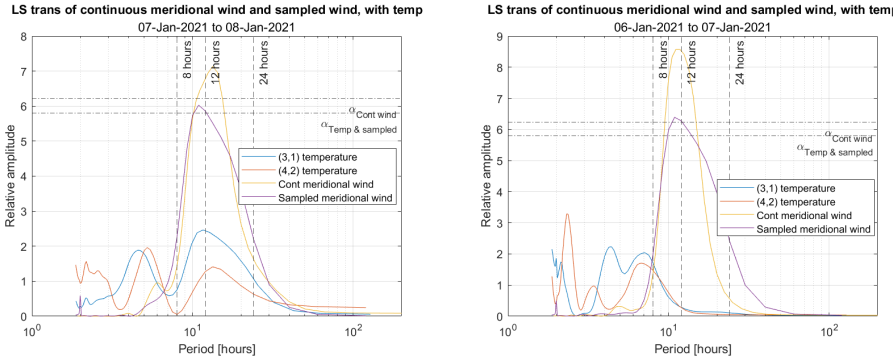

(a) Power spectrum where the temperature transforms match the sampled wind.

(b) Power spectrum where the temperatures do not match the sampled wind that night.

Figure 4.8: Examples of how the same temperatures and meridional wind do not necessarily produce the same tides, seen for two subsequent nights.

4.2.3 The effect of meteor counts on the weighted meridional wind

In this analysis, the meridional wind has been used as a golden standard. However, since the weighted meridional wind is calculated on an hourly average, the error for each calculated point in time will depend on the number of meteors at each altitude. Klemsdal 2015 presents results showing how the error in the wind estimate increases logarithmically when the number of meteors used in the calculations decreases to below 50 counts an hour. The weighted wind will on an hourly calculation be exposed to inaccuracies and high uncertainties in the contributions from wind contributions at altitudes with periodically fewer meteors.

deWit et al. 2015 presents how the number of meteors entering the atmosphere and being measured by the SKiMET radar varies seasonally and daily. The time of day the meteor intensity is maximum and minimum varies through the year. The meteor count in the upper atmosphere is maximum during the early morning, from three to nine, and is lowest between two and six during the afternoon. This can be seen in figure 3.4, where it is clear that the measurable number of meteors entering at different altitudes varies cyclically over 24 hours.

Such varying errors in the data might have the same effect on the derivation of tides as the nightly sampling of OH does. Parts of the data with a high uncertainty can affect the results in almost the same way as missing data, as it can include incorrect or misleading tides compared to the actual tides.

As can be seen in figure 3.4, some of the altitudes experience meteor counts less than the limit of 50 counts per hour, each evening. Therefore, these wind measurements will contribute uncertain winds to the total weighted wind. The error in the result will depend on that altitude's weight in the weight function, where the altitudes closer to 88km contribute

more.

Data presenting uncertain results can be treated the same way missing data points affect a non-continuous time series. If one only considers meridional wind data with measurements with low error, the meridional wind will experience an effect similar to sampling the OH. Therefore, potential sampling effects should be considered when deriving tides from a continuous meridional wind time series. The number of meteors used in the measurement of the wind should always be included in a wind analysis, as sampling affects the tides derived.

4.2.4 The effect of sampling time and length of time series

These results show how the sampling effect affects the tides presented in a power spectrum. The examples are calculated based on data from different seasons and a different number of consecutive days. The number of days and the length of the night (i.e. the season) affects the Lomb-Scargle transform and the resolution and confidence level of the sampled wave. This can be seen by comparing the power spectrum of a continuous and sampled sine wave with periods of 8 hours, 12 hours and 24 hours based on five days in January compared to 3 days in January, and the same when using five days in April and three days in April. The result can be seen in figure 4.9. This shows how the resolution in the periods is better for both the sampled wave and continuous wave when five days is used (figure 4.9a, figure 4.9c). When considering a fewer number of days, the resolution becomes worse, and the periods returned by the sampled wave do not reach the 95% confidence level. Extra tides appear for the sampled signal with just three days in April, figure 4.9d. These results make it clear that the length of the time series and the sampled time available affect the frequency analysis.

To investigate the sampled time and length of time series' effect on the sampled signal, the correlation coefficient between the LS-transform of a continuous sine wave and a sine wave sampled during the night was calculated. The sine wave was constructed based on the length of the continuous meridional wind time series and was a superpositioned wave with periods of 8 hours, 12 hours and 24 hours. The sampled wave was the same sine wave but with data at the times when the OH was sampled. The length of nights was varied along with the number of consecutive nights. The length of night was varied from January, where a night was as long as 17 hours, to April, where it was 7 hours long. The number of consecutive nights was changed from 1 night to 4 nights.

The result can be seen in figure 4.10. The plot shows a clear connection between the number of successive days used in the time series and the length of available sampled OH data, and the sampled waves' ability to represent the tides in the continuous time series. These factors play a role in how accurate the tides derived from the sampled signal are compared to the tides derived from the continuous signal. A tide can be derived using only one night if one uses data sampled during a season where the nights are long. If the data is sampled during spring or summer, where the nights are shorter, it is necessary to have

at least three or four consecutive nights of data to trust the results. A similar study should be done with a sine wave containing only one major tide, either an 8-hour, 12-hour, or a 24-hour period. The aim should be to investigate the sampling effect on a series with only one period.

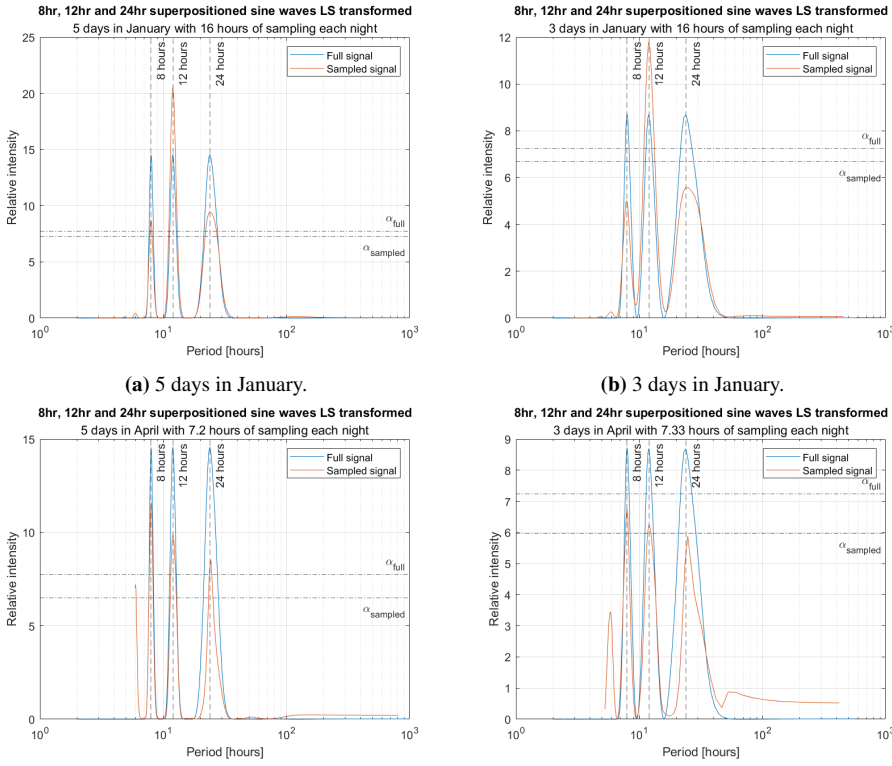

(a) 5 days in January.

(b) 3 days in January.

(c) 5 days in April.

(d) 3 days in April.

Figure 4.9: The Lomb-Scargle transformed sine waves with periods of 8 hours, 12 hours and 24 hours. A continuous and sampled time series spanning 3 days and 5 days in January and April were used, illustrating the sampled effect on the frequency analysis.

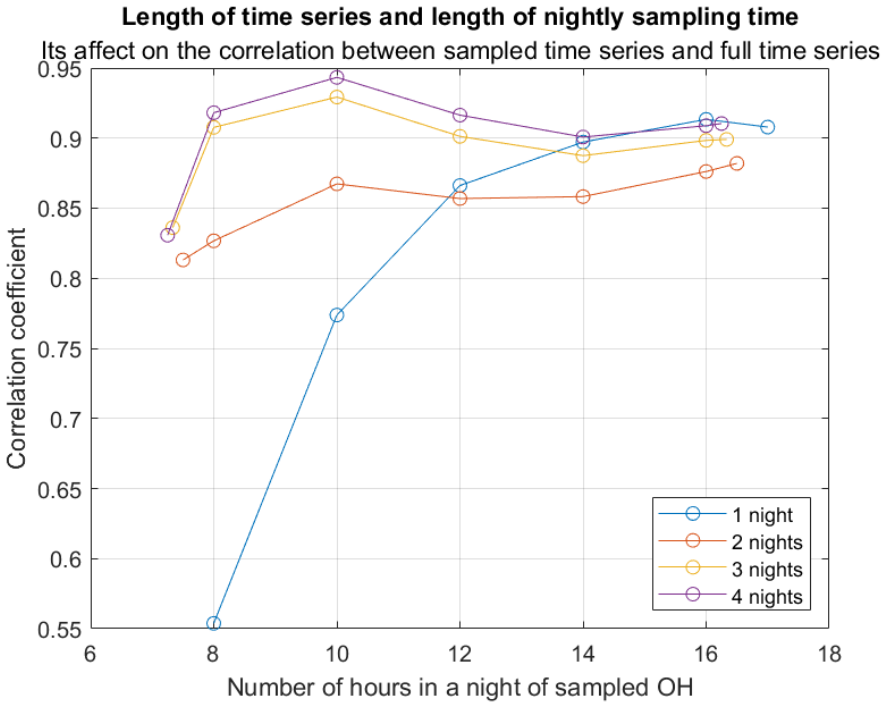

Figure 4.10: The accuracy of the sampled time series power spectrum compared to the periods returned when analysing a continuous time series. The number of consecutive days used and the length of the nights was varied.

Chapter 5

Conclusion

This master's thesis aimed at calculating the temperatures of the (3,1) and (4,2) Meinel bands. As a continuation, an analysis of the viability of using non-continuous time series to derive tides was conducted. The temperatures were calculated by fitting Gaussian line shapes to the OH intensity spectra at 15-minute intervals. When this fit was sufficiently good, evaluated by looking at the root mean square error of the fit, the resulting temperature calculations were in accordance with previous studies. Future temperature calculations should focus on the fitting of the Gaussian line shapes. Generally, bad fits occurred when there was a lot of noise in the intensity spectra. Using a filter to smooth the OH intensity spectrum might make it easier to fit the Gaussians. In addition, more research on how to make sure the program isolates the correct peaks in the spectrum should be conducted. As stated, the peaks in the intensity spectrum take the shape of a shifted Gaussian rather than a pure Gaussian. To increase the fit, incorporating a shifted Gaussian into the existing program could be done. In addition to this, some research should be conducted on the variation in the OH intensity and the temperatures. Since the temperature depends on the measured OH intensity of the different branches, some research should be conducted to show how the intensity of these branches changes through the night. It is known that the Q-branches of the OH (3,1) and (4,2) Meinel bands have varying standard variations. Research into similar effects on the different P-branches might be worth investigating.

Evaluating the tides in the temperatures was nearly impossible for more extended time series. By using hourly averages, geophysical and statistical noise effects were dampened, but most of the peaks in the power spectrum were still well below the 95% confidence level, and it was difficult to interpret the spectrum. By looking at how the sampling of OH during the night affected the resulting power spectrum, it was concluded that sampling data will lead to artificial tides in the power spectrum. This is inconvenient as it affects most of the tides derived from OH data, as all OH data has been sampled during the night. It was discovered that sine waves with noise could be used to approximate the measured tides.

Using sine waves combined with meridional wind measurements would make it possible to create a data bank of the sampled power spectrum shapes. This could be used to compare the shape a sampled time series takes in a power spectra and then appropriate the correct tide to the limited time series. If more research is conducted, it might be possible to derive tides from non-continuous time series in the atmosphere, such as time series produced by a spectrometer. This method is cheaper than using continuous time series produced by meteor radars. To do this, it is necessary to compare with data such as the continuous wind series. More research into the effect winds at altitudes with periodically low meteor count have on the weighted wind series should be conducted. The aim should be to discover if and how much of a sampling effect a low meteor count has and how this affects the derivation of tides in the weighted meridional wind.

In addition to this, results dictating the necessary length of sampling time, i.e. the length of the night, and the necessary number of consecutive days included in the time series, were presented. One either needs one long night lasting fourteen or more hours or three to four consecutive nights lasting more than eight hours. This should be used to assess the reliability of previous studies and assist forthcoming studies using non-continuous time series and data sampled at specific times to derive tides. A similar study using sine waves with only an eight hour period, twelve hour period, and a twenty-four hour period, as opposed to a sum of all periods, should be conducted to evaluate how a sampling affects a series with fewer dominating periods.

Bibliography

[Andrews 2010] David G. Andrews (2010). *An Introduction to Atmospheric Physics, Second Edition*. ISBN: 978-0-521-69318-9.

[N.d.] *Atmospheric Structure* (n.d.). URL: https://www.albany.edu/faculty/rgk/atm101/structur.htm.

[Baker et al. 2001] D. N. Baker et al. (Nov. 2001). "Relationships between precipitating auroral zone electrons and lower thermospheric nitric oxide densities: 1998-2000". In: *Journal of Geophysical Research: Space Physics* 106.A11, pp. 24465–24480.

[Berge and P. J. Espy 2011] F. T. Berge and P. J. Espy (2011). "Development of a spectrometer system to remotely sense mesospheric temperature". Trondheim: Norwegian Institudeof Science and Technology.

[deWit et al. 2015] R. J. deWit, R. E. Hibbins, and P. J. Espy (May 2015). "The seasonal cycle of gravity wave momentum flux and forcing in the high latitude northern hemisphere mesopause region". In: *Journal of Atmospheric and Solar-Terrestrial Physics* 127, pp. 21–29. ISSN: 13646826. DOI: 10.1016/J.JASTP.2014.10.002.

[P J Espy and Hammond 1995] P J Espy and M R Hammond (1995). "Atmospheric transmission coefficients for hydroxyl rotational lines used in rotational temperature determinations". In: *J. Quant. Spectrosc. Radial. Tmnsfer* 54.5, pp. 879–889.

[P J Espy and Stegman 2002] P J Espy and J Stegman (2002). "Trends and variability of mesospheric temperature at high-latitudes". In: *Physics and Chemistry of the Earth* 27, pp. 543–553.

[P. J. Espy et al. 2003] P. J. Espy et al. (Mar. 2003). "Rapid, large-scale temperature changes in the polar mesosphere and their relationship to meridional flows". In: *Geophysical Research Letters* 30.5, p. 1240. ISSN: 1944-8007. DOI: 10.1029/2002GL016452.

[Franzen et al. 2020] Christoph Franzen, Patrick Espy, and Robert Hibbins (Jan. 2020). "Modelled effects of temperature gradients and waves on the hydroxyl rotational dis-

tribution in ground-based airglow measurements". In: *Atmospheric Chemistry and Physics* 20.1, pp. 333–343. ISSN: 16807324. DOI: 10.5194/acp-20-333-2020.

[Fritts and Alexander 2003] David C. Fritts and M. Joan Alexander (Mar. 2003). "Gravity wave dynamics and effects in the middle atmosphere". In: *Reviews of Geophysics* 41.1. ISSN: 1944-9208. DOI: 10.1029/2001RG000106.

[Hedin 1991] A. E. Hedin (Feb. 1991). "Extension of the MSIS Thermosphere Model into the middle and lower atmosphere". In: *Journal of Geophysical Research: Space Physics* 96.A2, pp. 1159–1172. ISSN: 2156-2202. DOI: 10.1029/90JA02125.

[Hemmer 2005] P C Hemmer (2005). *Kvantemekanikk*. 5th ed. ISBN: 9788251920285.

[Hennum and P. Espy 2013] E Hennum and P Espy (2013). "A new algorithm for remote sensing mesopause temperatures using the hydroxyl airlgow". Trondheim: Norwegian Institudeof Science and Technology.

[Herzberg 1971] Gerhard Herzberg (1971). *The Spectra and Structures of Simple Free Radicals*.

[Hibbins et al. 2007] R. E. Hibbins et al. (Apr. 2007). "A climatology of tides and gravity wave variance in the MLT above Rothera, Antarctica obtained by MF radar". In: *Journal of Atmospheric and Solar-Terrestrial Physics* 69.4-5, pp. 578–588. ISSN: 13646826. DOI: 10.1016/J.JASTP.2006.10.009.

[Hocking 2001] W. K Hocking (2001). *Buoyancy (gravity) waves in the atmosphere*. URL: https://physics.uwo.ca/~whocking/p103/grav_wav.html.

[Image Analyst n.d.] Image Analyst (n.d.). *Fit Multiple Gaussians*. URL: https://se.mathworks.com/matlabcentral/fileexchange/74408-fit-multiple-gaussians/.

[Klemsdal 2015] Thor Olaf Klemsdal (2015). "What determines the wind uncertainty in a meteor wind radar?" NTNU.

[Lindzen 1979] R S Lindzen (1979). "Atmospheric Tides". In: *Ann. Rev. Earth Planet. Sci* 7, pp. 199–225. URL: www.annualreviews.org.

[Lowe et al. 1996] R P Lowe, L M Leblanc, and K L Gilbert (1996). *WINDII/UARS observation of twilight behaviour of the hydroxyl airglow, at mid-latitude equinox*. Tech. rep. 16, pp. 1863–1869.

[Marsh et al. 2006] Daniel R. Marsh et al. (Oct. 2006). "SABER observations of the OH Meinel airglow variability near the mesopause". In: *Journal of Geophysical Research: Space Physics* 111.A10, pp. 10–15. ISSN: 2156-2202. DOI: 10.1029/2005JA011451.

[Meinel 1950] A B Meinel (1950). "OH emission bands in the spectrum of the night sky". In: *The Astrophysical Journal* 111, p. 555.

[Mohr 2021] Kristine Biering Mohr (2021). *Coupling of OH radiation and meridional wind in the mesosphere and lower thermosphere*. Tech. rep. NTNU.

[Mulligan et al. 1995] F. J. Mulligan et al. (Nov. 1995). “Mesopause temperatures and integrated band brightnesses calculated from airglow OH emissions recorded at Maynooth (53.2°N, 6.4°W) during 1993”. In: *Journal of Atmospheric and Terrestrial Physics* 57.13, pp. 1623–1637. ISSN: 0021-9169. DOI: 10.1016/0021-9169(94)00133-9.

[Nappo 2013] C. J Nappo (2013). *An Introduction to Atmospheric Gravity Waves*. 2nd ed. Academic Press.

[Rothman et al. 2013] L. S. Rothman et al. (Nov. 2013). “The HITRAN2012 molecular spectroscopic database”. In: *Journal of Quantitative Spectroscopy and Radiative Transfer* 130, pp. 4–50. ISSN: 0022-4073. DOI: 10.1016/J.JQSRT.2013.07.002.

[Sivjee 1992] G. G. Sivjee (Feb. 1992). “Airglow hydroxyl emissions”. In: *Planetary and Space Science* 40.2-3, pp. 235–242. ISSN: 0032-0633. DOI: 10.1016/0032-0633(92)90061-R.

[N.d.] *Soloppgang og solnedgang i Trondheim* (n.d.). URL: https://www.timeanddate.no/astronomi/sol/norge/trondheim.

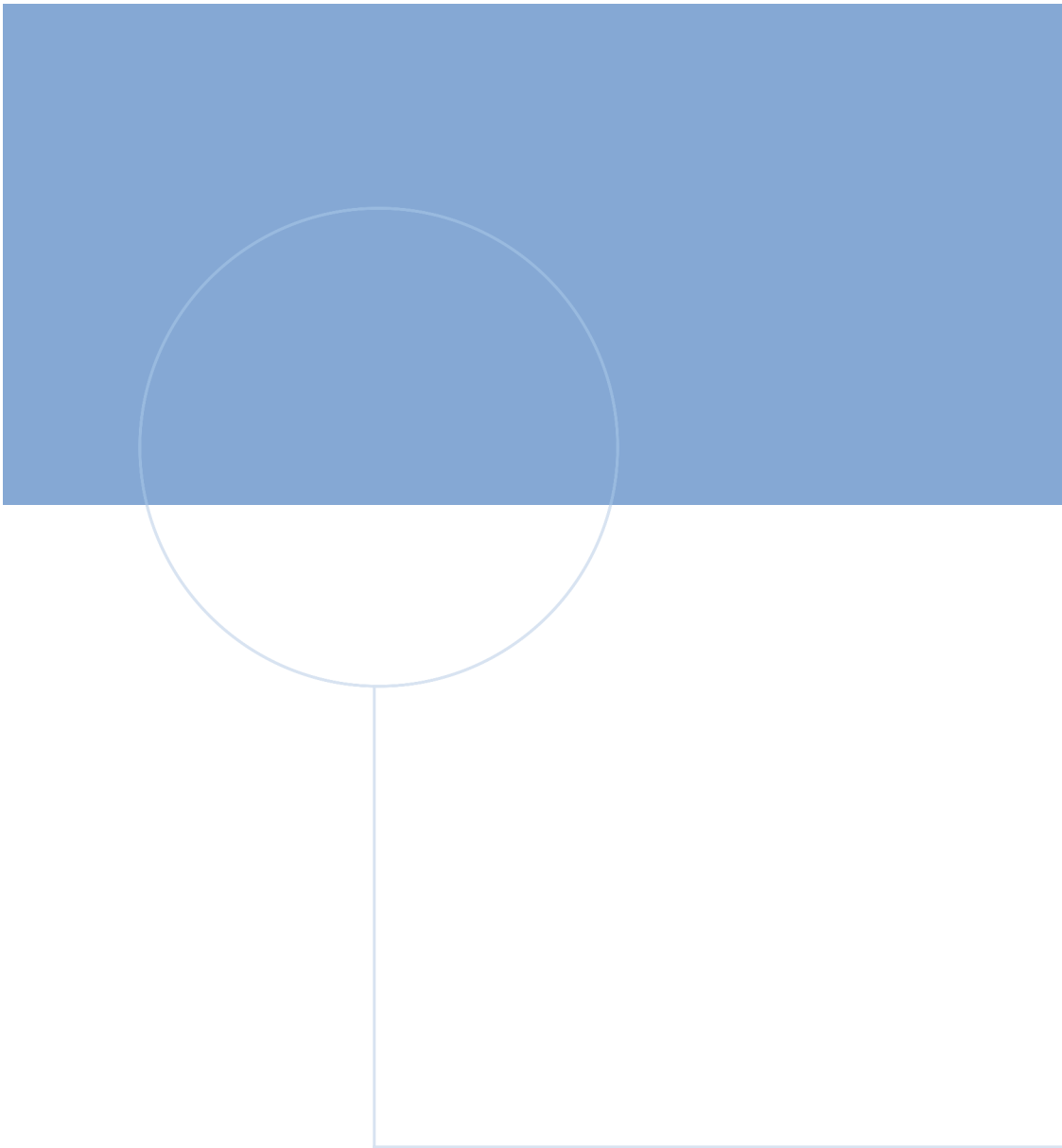

NTNU

Kunnskap for en bedre verden